Study of neutrino interactions in hydrogen and deuterium.
II. Inelastic charged-current reactions

S. J. Barish,* M. Derrick, T. Dombeck,† L. G. Hyman, K. Jaeger, B. Musgrave, P. Schreiner, R. Singer, and
A. Snyder

Argonne National Laboratory, Argonne, Illinois 60439

V. E. Barnes, D. D. Carmony, and A. F. Garfinkel

Purdue University, Lafayette, Indiana 47907
(Received 13 October 1978)

This paper gives the results of a study of inelastic charged-current interactions of muon-type neutrinos with hydrogen and deuterium targets using the Argonne 12-foot bubble chamber. We discuss in detail the separation of the events from background. For the single-pion production reactions $\nu p \to \mu^- p \pi^+$, $\nu n \to \mu^- n \pi^+$, and $\nu n \to \mu^- p \pi^0$, energy-dependent cross sections, differential cross sections, invariant-mass distributions, and the $\Delta^{++}(1236)$ decay angular distribution are presented. These data are also used to study the isospin properties of the πN system. Comparisons of the data with models of single-pion production are made, and a direct test of partial conservation of the axial-vector current is discussed. Cross sections and invariant-mass distributions are given for the reactions in which more than one pion is produced. Ten events of strange-particle production were found, and the properties of these events are discussed. The energy dependence of the total νp and νn cross sections from threshold to 6 GeV was determined, and the $\sigma(\nu n)/\sigma(\nu p)$ ratio measured. This ratio and the inclusive x and y distributions rapidly approach the scaling distributions expected from the quark-parton model.

I. INTRODUCTION

In this paper we present results on pion production in charged-current (CC) neutrino reactions from an experiment using the Argonne National Laboratory 12-ft bubble chamber filled with hydrogen and deuterium. Details of the experimental arrangement have been discussed in a previous article,[1] and preliminary results on single-pion production have been presented.[2] In this paper, we describe the event-selection procedures and discuss the final results from the present experiment. A larger exposure of the deuterium-filled chamber has been made to the neutrino beam, and the data from this second experiment are being processed.[3] The exclusive CC reactions studied are listed in Table I. Most of the data come from the deuterium exposure, although results from a small run with a hydrogen filling of the bubble chamber are also included. The paper is divided into four topics: single-pion reactions, multipion reactions, strange-particle production, and inclusive distributions.

In the neutrino-beam energy region below 6 GeV in which our data are concentrated, it is presently accepted that the weak hadronic CC contains only vector and axial-vector components. The hypothesis of the isotriplet vector current directly relates the weak hadronic vector current to the isovector electromagnetic current. The latter current has been well measured in electroproduction reactions, so a principal physics interest in our experiment is to measure the details of the weak hadronic axial-vector current. At higher energies the quark-parton model (QPM) has provided a unifying theme for lepton scattering experiments, and it is therefore of interest to see to what extent our low-energy inclusive distributions follow the expectation of this model.

II. EVENT SELECTION FOR SINGLE-PION PRODUCTION REACTIONS

A. The reaction $\nu p \to \mu^- p \pi^+$

In order to examine events belonging to reaction (1) (see Table I) and to estimate possible background contamination, we consider one-constraint kinematic fits to the reaction

$$xp \to \mu^- p \pi^+ ,$$

where x is a particle of zero mass with unknown vector momentum. Figure 1(a) displays a scatter plot of the azimuthal angle versus the dip angle for all events in the hydrogen sample with a χ^2 fit probability $\geq 1\%$. The nominal neutrino-beam direction is $0°$ for both variables with an uncertainty of $\pm 1°$. Strong clustering is seen at the position expected for neutrino-induced events. Figure 1(b) displays the identical plot for events in deuterium. A concentration near $\phi = \lambda = 0$ is again visible, although now it is broader due to the unmeasured vector momentum of the neutron spectator. Most of the other events in these plots are either examples of multipion production by neutrinos or events induced

TABLE I. The exclusive channels that form the inclusive reactions $\nu + p \rightarrow \mu^- + X^{++}$ and $\nu + n \rightarrow \mu^- + X^+$.

Reaction	Corrected No. of events in H_2	Corrected No. of events in D_2
(1) $\nu p \rightarrow \mu^- p \pi^+$	90 ± 11	308 ± 24
(2) $\nu p \rightarrow \mu^- p \pi^+ (l\pi^0)$, $l \geq 1$	5 ± 3	20 ± 5
(3) $\nu p \rightarrow \mu^- n \pi^+ \pi^+ (m\pi^0)$, $m \geq 0$	2 ± 1	15 ± 5
(4) $\nu p \rightarrow \mu^- p \pi^+ \pi^+ \pi^-$	0	10 ± 3
(5) $\nu p \rightarrow \mu^- p \pi^+ \pi^+ \pi^- \pi^0$		
(6) $\nu p \rightarrow \mu^- n \pi^+ \pi^+ \pi^+ \pi^-$	2 ± 1	1 ± 1
(7) $\nu p \rightarrow \mu^- +$ strange particles	3 ± 3	1 ± 1
(8) $\nu n \rightarrow \mu^- p$		833 ± 41
(9) $\nu n \rightarrow \mu^- p \pi^0$		124 ± 14
(10) $\nu n \rightarrow \mu^- n \pi^+$		90 ± 11
(11) $\nu n \rightarrow \mu^- p (k\pi^0)$, $k \geq 2$		31 ± 13
(12) $\nu n \rightarrow \mu^- n \pi^+ (l\pi^0)$, $l \geq 1$		29 ± 12
(13) $\nu n \rightarrow \mu^- p \pi^+ \pi^-$		20 ± 5
(14) $\nu n \rightarrow \mu^- p \pi^+ \pi^- (l\pi^0)$, $l \geq 1$		8 ± 4
(15) $\nu n \rightarrow \mu^- n \pi^+ \pi^+ \pi^- (m\pi^0)$, $m \geq 0$		3 ± 2
(16) $\nu n \rightarrow \mu^- p \pi^+ \pi^+ \pi^- \pi^-$		0
(17) $\nu n \rightarrow \mu^- +$ strange particles		12 ± 4

by incident charged hadrons that scatter in the chamber liquid; the number of weak-neutral-current events and neutron-induced events present is small.

The event samples were isolated by kinematically fitting all events to the $\mu^- p \pi^+$ final state. For the hydrogen sample, three-constraint (3C) fits were performed since the neutrino-beam direction is known. For the deuterium case, each of the neutron-spectator momentum components p_x, p_y, and p_z was given a starting value of 0 ± 50 MeV/c and 3C fits were again performed. A total of 82 and 249 fits were obtained in hydrogen and deuterium, respectively. Because of secondary scatters near the primary vertex, 9% of the fits were reduced to two-constraint. The π^+/p mass ambiguity between the positive tracks was resolved wherever possible by using visual information such as ionization density, particle decays, and secondary interactions; the 1% of the events which remained ambiguous were resolved by taking the fit with higher χ^2 probability. After these selections and with a 1% χ^2-probability cut, the background in the data samples is ~2% and 5%, respectively. These numbers were obtained by extrapolating the background, as determined using the data in Fig. 1,

into the region near the origin.

The background from multipion production by neutrinos [reactions (2) and (3)] was independently estimated by taking a sample of events classified as belonging to reactions (4) to (6) and (13) to (16), deleting one or more charged-hadron tracks, and attempting to fit them to the $\mu^- p \pi^+ n$ final state. Above $E_\nu = 1.0$ GeV, the background from this source was found to be ~2% and did not populate any particular regions of q^2 or the $p\pi^+$ effective mass.

Because of the 0 ± 50 MeV/c starting value that was given to the momentum of the neutron spectator, events in deuterium with a fast neutron spectator often fail to give an acceptably high χ^2 probability. In order to correct the cross section for this loss, we considered events that had been identified as the reaction $\nu d \rightarrow \mu^- p p_s$ and for which the spectator is seen. Figure 2(a) displays the momentum distribution of the proton spectator for this data sample. We discarded the measurements of the proton spectators and refit the events using starting values of 0 ± 50 MeV/c for the spectator momentum. Events giving a successful fit are shown cross-hatched in Fig. 2(a). The fitted spectator momentum distribution for these events is
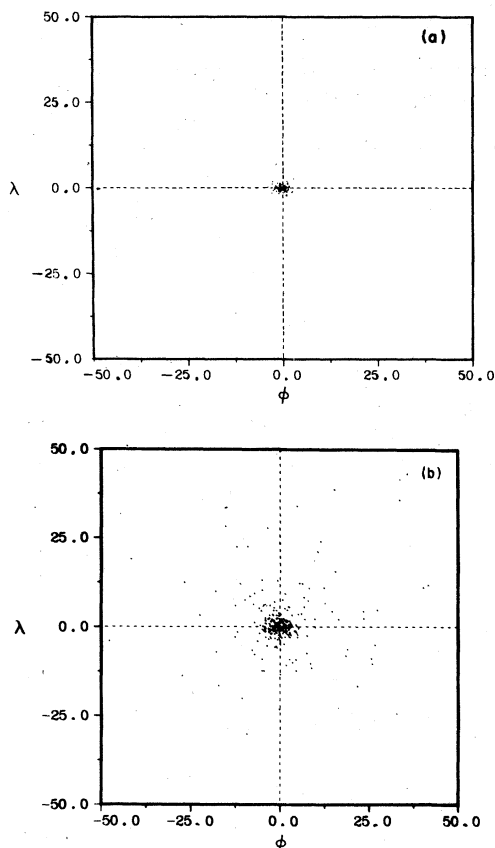
FIG. 1. Scatter plot of the azimuth angle ϕ against the dip angle λ for events of the reactions: (a) $xp \to \mu^-p\pi^+$ and (b) $xd \to \mu^-p\pi^+n_s$ where the mass of the particle x is assumed to be zero. A clear clustering of events is seen at $\lambda=\phi=0$ corresponding to the true neutrino-induced events.

FIG. 2. (a) The distribution in momentum for the visible proton spectators in the reaction $\nu d \to \mu^-pp_s$. The cross-hatched events are those giving fits to the μ^-pp_s hypothesis when the kinematic information of the spectator track is discarded. (b) The fitted spectator momentum distribution for the events cross-hatched in (a).

shown in Fig. 2(b) and is displaced to lower momentum values. In addition, we found that 15% of the events failed to give a fit with χ^2 probability greater than 1%.

If the true spectator momentum distributions in the reaction $\nu d \to \mu^-p\pi^+n_s$ and $\nu d \to \mu^-pp_s$ were identical, we should scale up our $\mu^-p\pi^+n_s$ cross section by this same factor of 15%. However, since the number of fast spectators which come from rescattering increases as the number of strongly interacting particles in the final state, an additional 4% correction has been applied. This additional factor was obtained from a simple model of πp and pp elastic scattering in the final state. The 15% correction factor was studied as a function of the neutrino energy. There is a suggestion that the loss of fits increases as the energy increases, but to within the errors of the analysis, there is no energy dependence. The events lost from the $\mu^-p\pi^+$ channel are all misclassified as belonging to the
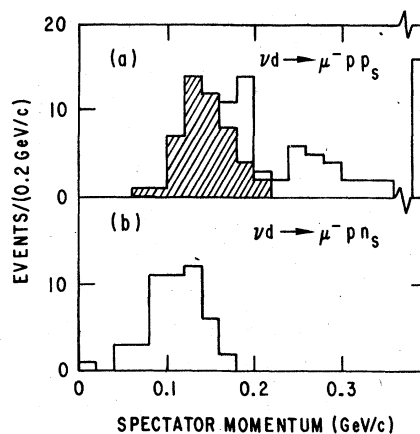
reaction $\nu d \to \mu^-p\pi^+\pi^0n_s$. This contamination in the 2π data sample is discussed in a later section of the paper. All the film was double-scanned and the events were measured several times if necessary, giving resulting efficiencies in the range 97% to 99%.

Table II summarizes the corrections which have been used to obtain absolute cross sections for reaction (1). The corrections are independent of the neutrino energy. The cross sections for the reaction $\nu p \to \mu^-p\pi^+$ measured in the hydrogen exposure and in the deuterium exposures are in satisfactory agreement.

B. The reactions $\nu d \to \mu^-p\pi^0p_s$ and $\mu^-n\pi^+p_s$

The selection of events for $\nu n \to \mu^-p\pi^0$ [reaction (9)] and $\nu n \to \mu^-n\pi^+$ [reaction (10)] is more difficult since the equations of energy-momentum balance are not overconstrained. However, in resolving kinematical ambiguties between the $\mu^-p\pi^0$ and $\mu^-n\pi^+$ final states, we make use of visual information such as track shape, ionization density, par-

TABLE II. Rate corrections for $\nu p \to \mu^-p\pi^+$.

Reason for correction	Correction factor	
	H_2	D_2
Background	0.98 ± 0.01	0.95 ± 0.03
Loss of fast-neutron spectators	1.00	1.23 ± 0.06
Double-scan efficiency	1.02 ± 0.01	1.01 ± 0.01
Measuring and reconstruction efficiency	1.02 ± 0.02	1.03 ± 0.02

ticle decays, and secondary interactions.

An initial cut removes events fitting the $\mu^- p p_s$ or $\mu^- p \pi^+ n_s$ final states with χ^2 probability $\geqslant 1\%$. Because of the large number of incoming charged hadrons that scatter giving events which may easily satisfy the kinematics of reaction (10), additional selections were necessary. This background was only important for reaction (10) and then only for the two-prong events. The hadron-scattering events which fit the $\mu^- n \pi^+$ final state have an outgoing neutron of high momentum which is parallel to the neutrino-beam direction. Therefore, we only considered those fits for which both the angle between the incident neutrino and outgoing neutron θ_{vn} was greater than $10°$ and the neutron-to-neutrino momentum ratio (p_n/p_v) was less than 0.9. Although these selections removed most of the background, we added, in addition, a further requirement that the angle between the μ^- and π^+ tracks be less than $150°$. A study of a sample of events identified through three-constraint fits as hadron scatters showed that their misidentification as reaction (10) is completely precluded by application of the above selections. In order to estimate how many genuine examples of the $\mu^- n \pi^+$ final state are excluded by these cuts, the selection criteria were also applied to events identified as $vd \rightarrow \mu^- p \pi^+ n_s$, assuming the kinematics of the two single-pion production reactions are similar for low pion-nucleon masses. At the present level of statistics, no discernible bias in either the q^2 distribution or in the $\pi^+ n$ effective-mass distribution was introduced by these selection criteria.

In addition to the background from incident charged hadrons, background to reactions (9) and (10) arises from multipion production by neutrinos, neutron-induced processes, neutral-current reactions, and photo-induced processes. The photon is often associated with a cosmic-ray interaction.

The magnitude of the background from double-pion channels is estimated from a study of the reactions $vd \rightarrow \mu^- \pi^+ \pi^- p(p_s)$, $vd \rightarrow \mu^- \pi^+ \pi^- \pi^- n(p_s)$, $vp \rightarrow \mu^- \pi^+ \pi^+ n$, and $vp \rightarrow \mu^- \pi^+ \pi^0 p$. As shown in Sec. V, the excitation function for such reactions rises steeply and becomes comparable to the single-pion cross sections for neutrino energies greater than about 2 GeV. Furthermore, if the final states $\mu^- p \pi^0$ and $\mu^- n \pi^+$ are simulated by discarding charged hadron tracks from the above multipion reactions, the resulting calculated neutrino energy tends to remain above 1.5 GeV. Assuming that the multipion reactions proceed by isovector exchange with $\Delta(1236)$ dominance, the rates observed for the above multipion channels indicate total backgrounds in the single-pion final states of about 10%, provided that events with $E_v \leqslant 1.5$ GeV are selected.

The neutron-induced reactions $nn \rightarrow np\pi^-$ and nn

TABLE III. Rate corrections for the OC single-pion reactions.

Reason for correction	Correction factor
(a) $vd \rightarrow \mu^- p \pi^0 p_s$	
Double-scan efficiency	$1.02^{+0.01}_{-0.02}$
Measuring efficiency	1.02 ± 0.02
Loss of underconstrained events	1.04 ± 0.02
Events assigned to $\mu^- p p_s$	1.22 ± 0.05
Neutrino-multipion background	0.92 ± 0.03
Neutron-induced background	0.98 ± 0.02
Neutral-current background Photo-induced background	0.98 ± 0.02
(b) $vd \rightarrow \mu^- n \pi^+ p_s$	
Double-scan efficiency	$1.02^{+0.01}_{-0.02}$
Measuring efficiency	1.02 ± 0.02
Loss of underconstrained events	1.08 ± 0.02
Correction for $p_n/p_v > 0.9$ and $\theta_{vn} < 10°$	1.04 ± 0.02
Correction for $\theta_{\mu^- \pi^+} < 150°$	1.03 ± 0.02
Neutrino multipion background	0.90 ± 0.03
Neutron-induced background	0.99 ± 0.01
Neutral-current background Photo-induced background	0.99 ± 0.01

$\rightarrow nn\pi^+ \pi^-$ are also sources of background. The magnitude is estimated from that observed in the film for $np \rightarrow pp\pi^-$, together with known cross sections[1] for the charge-symmetric reactions $pp \rightarrow pn\pi^+$ and $pp \rightarrow pp\pi^+ \pi^-$.

The neutral-current process $vn \rightarrow vp\pi^-$, where the π^- leaves the chamber without interacting, can simulate the final state $\mu^- p \pi^0$. This background is estimated knowing the π^- detection efficiency as a function of momentum and the measured rate[4] for the $vp\pi^-$ final state. The photo-induced backgrounds are compiled from existing photoproduction cross sections, with the photon flux determined from e^+e^- pairs observed in the bubble chamber.

These and the other corrections appropriate to these final states are summarized in Table III. The correction for events that are underconstrained because of a track being too short to allow a momentum measurement is obtained from the sample of $\mu^- p \pi^+$ events.

A correction particular to the $\mu^- p \pi^0$ final state arises because events with a small π^0 transverse momentum relative to the neutrino-beam direction often give fits to the $\mu^- p$ final state and are so classified. The correction is measured by using events assigned to the $\mu^- p \pi^+$ final state, eliminating the π^+ track and fitting the event to the $vd \rightarrow \mu^- p \pi^0 n_s$ hypothesis. We measure that $(22 \pm 4)\%$ of the $\mu^- p \pi^0 p_s$ events are misclassified as quasielastic. We find two events with an associated e^+e^- pair

TABLE IV. Resolution for the 0C single-pion reactions.

Quantity	$\nu d \rightarrow \mu^- p \pi^0 p_s$	$\nu d \rightarrow \mu^- n \pi^+ p_s$
E_ν (GeV)	±0.06	±0.05
q^2 [(GeV/c)^2]	±0.02	±0.02
$M(N\pi)$ (GeV)	±0.05	±0.03

that fit the $\mu^- p p_s$ hypothesis consistent with this background estimate.

A further concern with these single-pion production events is the resolution in the kinematical quantities which is attained for these unconstrained channels. The resolution is studied using events assigned to the constrained $\mu^- p \pi^+$ final state. By removing the appropriate charged-particle track from the event, the $\mu^- p \pi^0$ and $\mu^- n \pi^+$ final states are simulated. The resulting uncertainties in E_ν, q^2, and $M(N\pi)$ are given in Table IV.

III. PHYSICS OF SINGLE-PION PRODUCTION

A. General properties of the $\mu^- p \pi^+$, $\mu^- p \pi^0$, and $\mu^- n \pi^+$ final states

We now display the data for the three single-pion production reactions. In Figs. 3, 4 and 5 we show

the $N\pi$, $N\mu^-$, and $\mu^- \pi$ effective-mass combinations, respectively. It is apparent that the $\mu^- p \pi^+$ final state is dominated by $\Delta(1236)$ production, with few events at high mass. That high-mass events are kinematically allowed can be seen in the $N\mu^-$ mass distributions of Fig. 4. In contrast to the situation for the $\mu^- p \pi^+$ final state, it is not obvious that Δ production dominates for the $\mu^- p \pi^0$ and $\mu^- n \pi^+$ channels. In particular, there is more evidence for high-mass $N\pi$ states than is seen for reaction (1) even though these data are limited to $E_\nu < 1.5$ GeV.

Figure 6 displays the energy distribution of the events. The spectrum peaks near 0.9 GeV; there is no evidence for fine structure. The corresponding cross sections are shown in Fig. 7 and listed in Table V after binning the data into six energy intervals. The error bars on the cross section contain both the overall normalization uncertainty of ±15% and a point-to-point relative error in the flux shape of ±5% folded in, except for the last point where we use ±15% to allow for the uncertainty in the K^+ flux. In calculating these cross sections, we have used the flux calculated from the measured pion production cross sections.

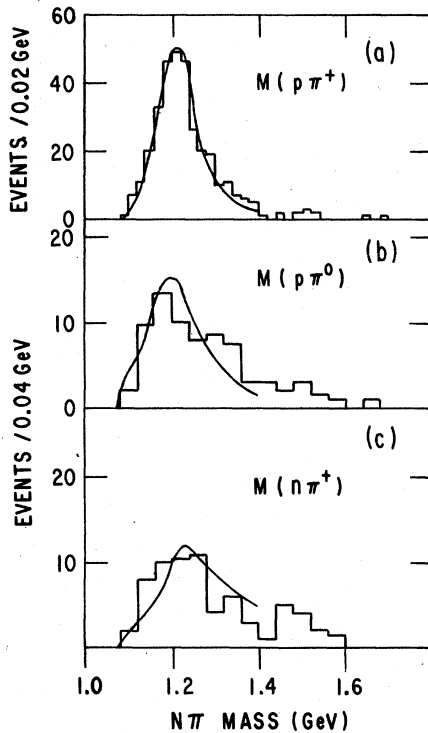Figure 8 shows the energy dependence of the cross section for the three single-pion reactions

FIG. 3. The $N\pi$ invariant-mass distribution for the final states (a) $\mu^- p \pi^+$, (b) $\mu^- p \pi^0$, and (c) $\mu^- n \pi^+$. The curves are the predictions of the Adler model, including the selection $E_\nu < 1.5$ GeV that has been made for (b) and (c).
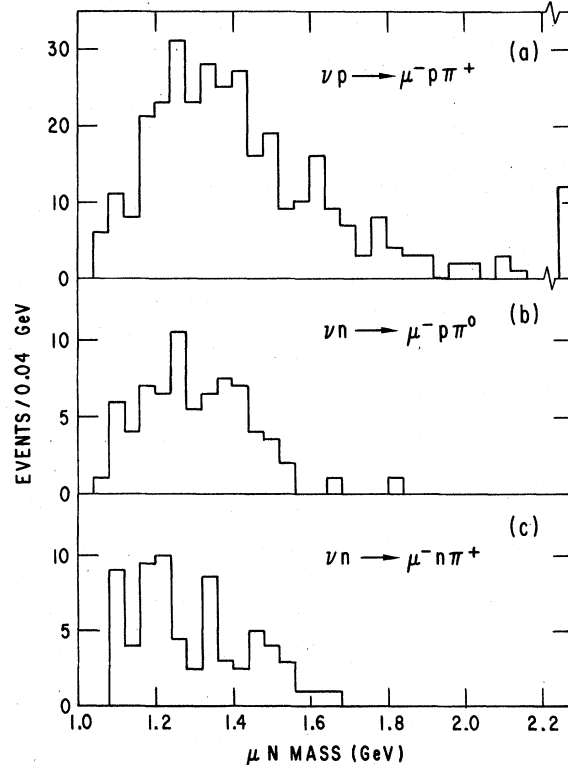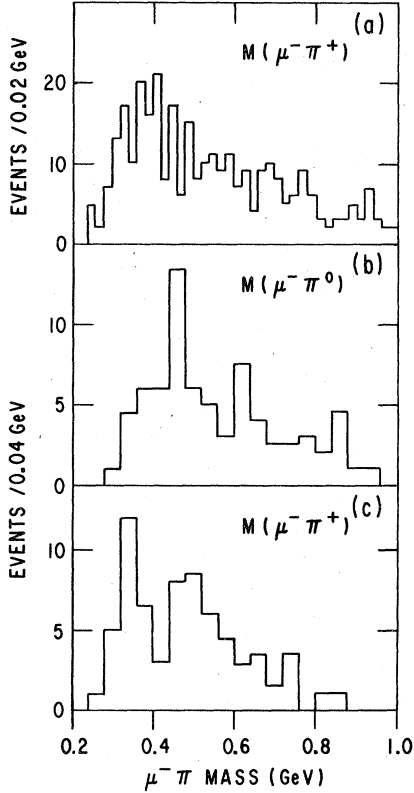

FIG. 4. The $\mu^- N$ invariant-mass distributions for the final states (a) $\mu^- p \pi^+$, (b) $\mu^- p \pi^0$, and (c) $\mu^- n \pi^+$.

FIG. 5. The $\mu^-\pi$ invariant-mass distributions for the final states (a) $\mu^-p\pi^+$, (b) $\mu^-p\pi^0$, and (c) $\mu^-n\pi^+$.
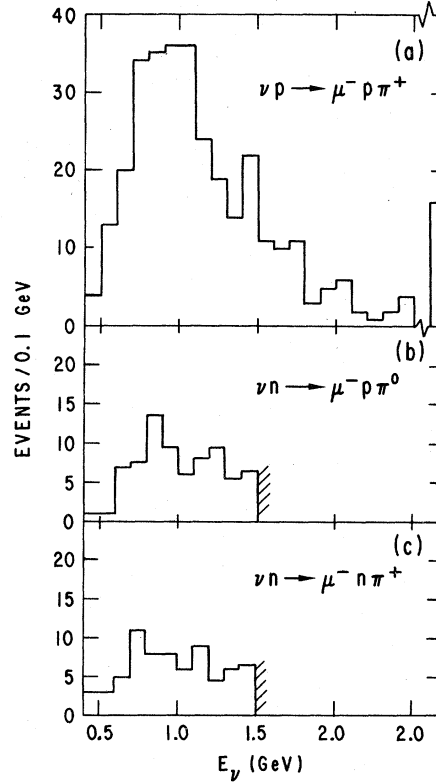

FIG. 6. The distribution of events in neutrino energy E_ν for the final states (a) $\mu^-p\pi^+$, (b) $\mu^-p\pi^0$, and (c) $\mu^-n\pi^+$. For the latter two reactions, the double-pion-production background requires the data to be cut off at $E_\nu = 1.5$ GeV.

with the selection $M(N\pi) \leqslant 1.4$ GeV; the data are also given in Table V. The mass selection restricts the data to the $\Delta(1236)$ mass region and permits comparisons with theoretical models as will be discussed below.

Figure 9 shows the $\cos\theta^*_{\nu\mu}$ distributions, where $\theta^*_{\nu\mu}$ is measured in the νN rest frame. The cross-hatched events in Fig. 9(b) show the correction required for events lost to the μ^-pp_s channel. Figure 10 gives the corresponding q^2 distributions with the events having $M(N\pi) \geqslant 1.4$ GeV or $E_\nu > 1.5$ GeV being cross hatched. The forward peaking of the μ^- comes entirely from the events above 1-GeV neutrino energy. This can be clearly seen in Fig. 11 which is a scatter plot of $\cos\theta^*_{\nu\mu}$ versus the neutrino-beam energy for the $\mu^-p\pi^+$ final state. At threshold, the Δ^{++} production angular distribution is nearly isotropic.

We examine the Δ^{++} decay angular distributions in the Adler coordinate system where the angles θ and ϕ are defined as in Fig. 12. The Δ^{++} is defined as $M_{p\pi^+} \leqslant 1.4$ GeV. The distributions are shown in Fig. 13; neither shows any striking structure. If time-reversal invariance holds in the Δ production process, the decay distribution is given by

$$\frac{d\sigma}{d\Omega} = \frac{\sigma}{\sqrt{4}}\left(Y_0^0 - \frac{2}{\sqrt{5}}\,(\tilde{\rho}_{33} - \tfrac{1}{2})\,Y_2^0 + \frac{4}{\sqrt{10}}\,\tilde{\rho}_{31}\,\mathrm{Re}\,Y_2^1 \right.$$

$$\left. - \frac{4}{\sqrt{10}}\,\tilde{\rho}_{3\text{-}1}\,\mathrm{Re}\,Y_2^2 \right),$$

where Y_L^M are spherical harmonic functions and $\tilde{\rho}_{mn}$ are the density matrix elements. This equation only applies in the absence of background, an approximation that is good for the Δ^{++} case. Table VI gives the experimental values for the three Δ^{++} density matrix elements for different $\cos\theta^*_{\nu\mu}$ and q^2 intervals. The $\tilde{\rho}_{mn}$ values plotted in Fig. 14 show some q^2 dependence. A check for the presence of "illegal" Y_L^M moments in the decay distribution was made (see Table VII); no terms were found that were significantly different from zero. In particular, the asymmetry in the $\cos\theta$ distribution of Fig. 13 is only a 2-standard-deviation effect.

B. Comparison of the $\mu^-\Delta^{++}$ final state with models

Many calculations have been made of the isospin $\tfrac{3}{2}$ amplitude, which determines the dominant struc-

ture of the $\mu^- p \pi^+$ final state. Preliminary data[5] from this experiment were used to test the predictions of models developed by Adler,[6] Zucker,[7] Salin,[8] Bijtebier,[9] and others. The very detailed calculations by Adler were found to agree well with all aspects of the data: $\sigma(E_\nu)$, $d\sigma/dq^2$, and $\tilde{\rho}_{mn}$.

For pure $\Delta(1236)$ production, the matrix element may be written in the form

$$H = \langle \mu^- \Delta^{++} | \nu p \rangle$$
$$= \frac{G}{\sqrt{2}} j_\alpha \langle \Delta^{++} | V^\alpha - A^\alpha | p \rangle ,$$

where $G = 0.99 \times 10^{-5} M^{-2}$ is the coupling constant for hypercharge-conserving semileptonic decays, $j^\alpha = \bar{u}_\mu \gamma^\alpha (1 - \gamma_5) u_\nu$ is the matrix element of the leptonic current, and $\langle \Delta^{++} | V^\alpha - A^\alpha | p \rangle$ is the matrix

element of the hadronic current separated into its vector and axial-vector parts.

The isotriplet-vector-current hypothesis states that the matrix elements of the weak strangeness-conserving hadronic vector-current are directly related to those of the $I = 1$ electromagnetic current measured in electroproduction by means of the relation

$$\langle \Delta^{++} | V^\alpha | p \rangle = \sqrt{3} \langle \Delta^+ | V_{\text{em}}^\alpha | p \rangle .$$

Thus, assuming the conserved-vector-current (CVC) hypothesis to hold, the interest in the neutrino experiment is to determine $\langle \Delta^{++} | A^\alpha | p \rangle$.

Using Rarita-Schwinger form factors, the matrix element may be written as a sum of eight terms:
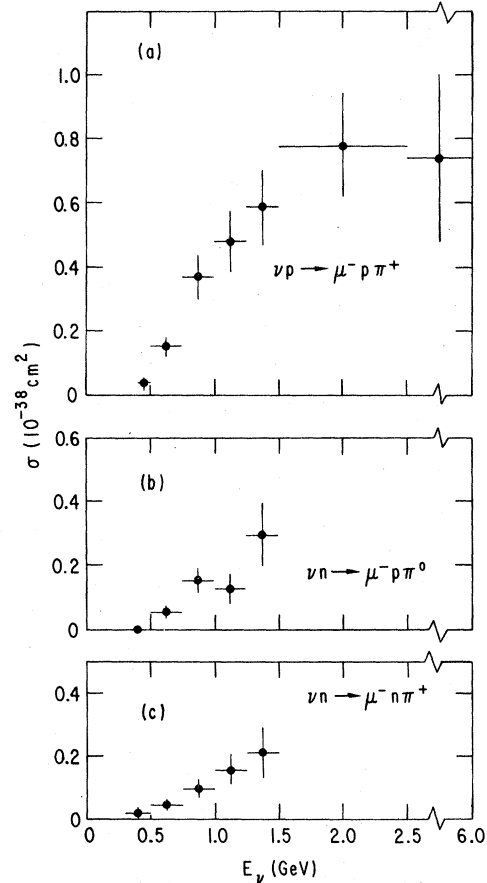
$$\langle \Delta^{++} | p \rangle = \frac{G}{\sqrt{2}} \psi_\alpha \left\{ \left[\frac{C_3^V}{M} \lambda_\gamma + \frac{C_4^V}{M^2} (P_\Delta)_\lambda + \frac{C_5^V}{M^2} (P_p)_\lambda \right] \gamma_5 F^{\lambda\alpha} + C_6^V j^\alpha \gamma_5 \right.$$
$$\left. + \left[\frac{C_3^A}{M} \gamma_\lambda + \frac{C_4^A}{M^2} (P_\Delta)_\lambda \right] F^{\lambda\alpha} + C_5^A j^\alpha + \frac{C_6^A}{M^2} (q)^\alpha q \cdot j \right\} uf(W) .$$

Here P_Δ is the Δ^{++} four-momentum, P_p is the proton four-momentum, M is the proton mass, $F^{\lambda\alpha} = q^\lambda j^\alpha - q^\alpha j^\lambda$, ψ_α is the Rarita-Schwinger spinor describing the Δ^{++} spin state, u is the Dirac spinor of the proton spin state, and f is an s-wave Breit-Wigner in the $N\pi$ invariant mass (W).

Time-reversal invariance is assumed to hold so that all the $C_i^{V,A}(q^2)$ form factors are relatively real. The CVC hypothesis and the approximation of magnetic-dipole dominance states that

$$C_4^V = -\frac{M}{W} C_3^V , \quad C_5^V = C_6^V = 0 .$$

The electroproduction data can be well fit by the following form for C_3^V:

$$|C_3^V|^2 = (2.05)^2 [1 + 9 (-q^2)^{1/2}] \exp[-6.3(-q^2)^{1/2}] .$$

In the partially conserved axial-vector current (PCAC) hypothesis, the axial-vector current is divergenceless in the limit where the pion mass goes to zero. Thus, one has

$$\langle \Delta^{++} | i \partial_\mu A^\mu | p \rangle = \sqrt{3} \bar{\psi}_\alpha q^2 \left[C_5^A + \frac{C_6^A}{M^2} q^2 \right] uf(W) .$$

The induced pseudoscalar form factor C_6^A contains a pion pole:

$$\frac{C_6^A(\text{pole})}{M^2} = \frac{g_\Delta f_\pi}{2\sqrt{3}M(m_\pi^2 - q^2)} ,$$

where $g_\Delta = 28.6$ is the $\Delta^{++} \to p\pi^+$ coupling constant and $f_\pi = 0.97 m_\pi$ is the pion decay constant. When $m_\pi^2 = 0$, this pole will give a nonvanishing contribu-

FIG. 7. The excitation functions for the final states (a) $\mu^- p \pi^+$, (b) $\mu^- p \pi^0$, and (c) $\mu^- n \pi^+$. No πN mass selection has been made for these data.

TABLE V. Energy dependence of the single-pion production cross sections.

E_ν (GeV)	$\sigma(\nu p \to \mu^- p \pi^+)$ (10^{-38} cm^2)		$\sigma(\nu n \to \mu^- p \pi^0)$ (10^{-38} cm^2)		$\sigma(\nu n \to \mu^- n \pi^+)$ (10^{-38} cm^2)	
	No cuts	$M(p\pi) < 1.4$ GeV	No cuts	$M(p\pi) < 1.4$ GeV	No cuts	$M(n\pi) < 1.4$ GeV
0.4 −0.5	0.036 ± 0.019	0.036 ± 0.19			0.02 ± 0.01	0.02 ± 0.01
0.5 −0.75	0.153 ± 0.033	0.153 ± 0.033	0.05 ± 0.02	0.05 ± 0.02	0.04 ± 0.02	0.04 ± 0.02
0.75−1.00	0.369 ± 0.069	0.364 ± 0.068	0.15 ± 0.04	0.14 ± 0.04	0.10 ± 0.03	0.09 ± 0.03
1.00−1.25	0.479 ± 0.094	0.471 ± 0.093	0.12 ± 0.05	0.09 ± 0.04	0.16 ± 0.05	0.10 ± 0.04
1.25−1.50	0.584 ± 0.127	0.540 ± 0.120	0.30 ± 0.10	0.23 ± 0.08	0.21 ± 0.08	0.12 ± 0.06
1.50−2.50	0.775 ± 0.160	0.696 ± 0.148				
2.50−6.00	0.739 ± 0.266	0.640 ± 0.239				

tion to the matrix element of the divergence

$$\langle \Delta^{++} | i\, \partial_\mu A^\mu | p \rangle \xrightarrow[\substack{m_\pi^2 = 0 \\ q^2 \to 0}]{} \sqrt{3}\, \bar{\psi}_\alpha q^2 u \left[C_5^A(0) - \frac{g_\Delta f_\pi}{2\sqrt{3}M} \right].$$

If the coupling constants g_Δ, f_π do not vary much from their physical values as $m_\pi^2 \to 0$, the matrix

element can be zero at $q^2 = 0$ when $m_\pi^2 = 0$ if

$$C_5^A(0) = \frac{g_\Delta f_\pi}{2\sqrt{3}M} = 1.2 \,.$$

In the Adler model, CVC and PCAC are assumed to hold. The excitation of the $\Delta(1236)$ occurs dominantly through the nucleon-exchange Born diagram shown in Fig. 15(a). Following Chew and Low, it is also assumed that higher-order effects are dominated by rescattering through the intermediate s-channel Δ state as
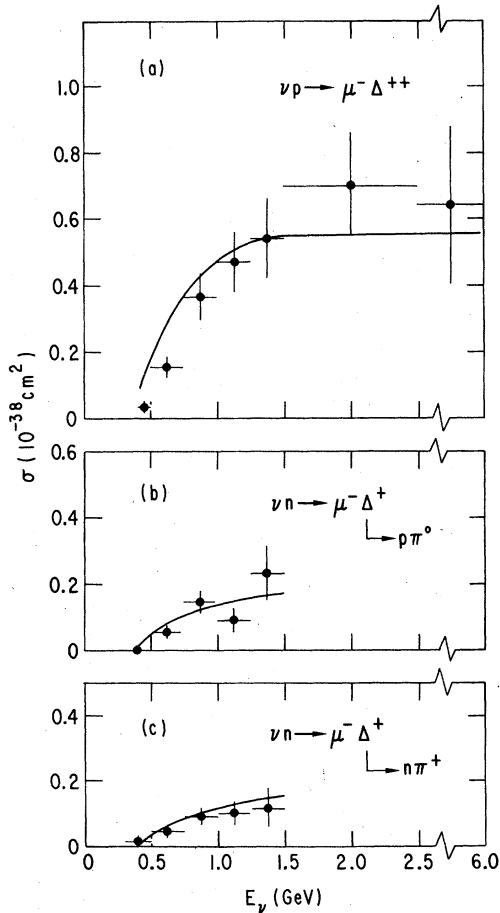

FIG. 8. The excitation functions for the final states (a) $\mu^- p \pi^+$, (b) $\mu^- p \pi^0$, and (c) $\mu^- n \pi^+$ with the selection $M(N\pi) < 1.4$ GeV. The curves show the comparison with the Adler model.
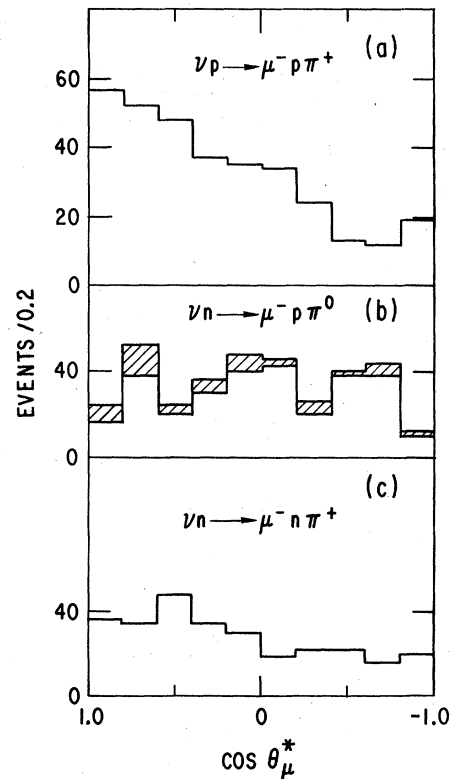

FIG. 9. The c.m. angular distributions for the final states (a) $\mu^- p \pi^+$, (b) $\mu^- p \pi^0$, and (c) $\mu^- n \pi^+$. The cross-hatched events in (b) show the correction for the events lost to the quasielastic channel.
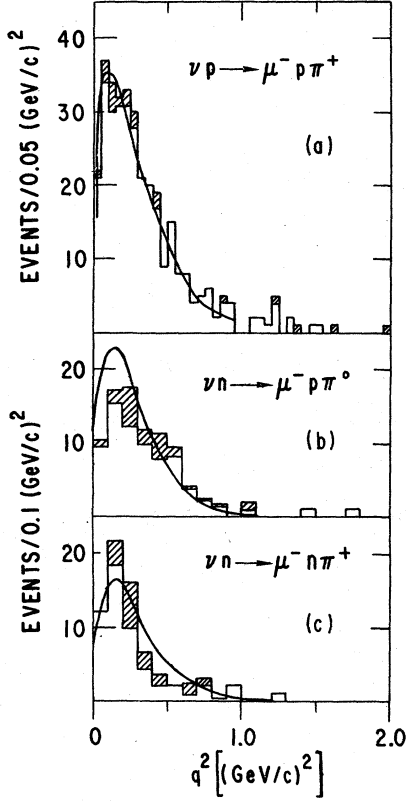
FIG. 10. The distributions in four-momentum transfer q^2 for the final states (a) $\mu^- p \pi^+$, (b) $\mu^- p \pi^0$, and (c) $\mu^- n \pi^+$. The open histogram corresponds to the events resulting from the selections $M(N\pi) < 1.4$ GeV and $E_\nu < 1.5$ GeV.
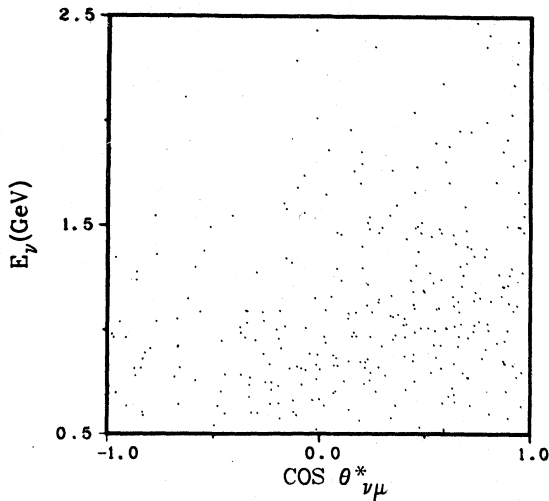

FIG. 11. Scatter plot of $\cos\theta^*_{\nu\mu}$ versus E_ν for events of the $\mu^- p \pi^+$ final state. The forward peaking only develops for the higher E_ν values.
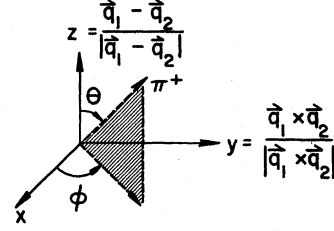

FIG. 12. Definition of the azimuthal ϕ and polar θ decay angles in the Adler system. $\vec{q}_1$ and $\vec{q}_2$ are vectors along the ν and μ^- direction respectively in the $N\pi$ rest system.

shown in Fig. 15(b). Because of the dominant nucleon-exchange terms, the q^2 dependences of the vector and axial-vector transition matrix elements are proportional respectively to the nucleon isovector magnetic and axial-vector form factors, multiplied by a more slowly varying factor coming from the q^2 dependence of the exchanged nucleon propagator. Table VIII lists the axial-vector couplings at $q^2 = 0$ in Adler's and Zucker's models. The coupling constants $C_3^A(0)$ and $C_4^A(0)$ are quite model-dependent. In all Δ production models, the axial-vector mass M_A is a free parameter.

To fit the $\mu^- p \pi^+$ data, we have used the following likelihood function:

$$L = D_1 D_2 D_3 ,$$

where

$$D_1 = \prod_{i=1}^{N_{\text{evts}}} \frac{d\sigma(E_i, W_i^2, q_i^2, \Omega_{\pi i})/dW^2 dq^2 d\Omega_\pi}{\sigma(E_i)} ,$$

$$D_2 = \prod_{j=1}^{6} \exp\left\{-[\sigma_j - \sigma_{\text{exp}}^R(j)]^2/2[\Delta\sigma^R(j)]^2\right\},$$

and

$$D_3 = \exp[-(\bar\sigma - \bar\sigma_{\text{exp}})^2/2(\Delta\bar\sigma)^2] .$$

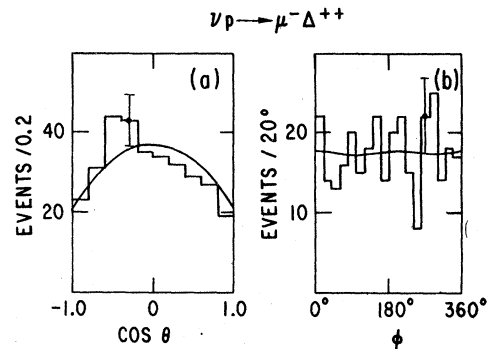Here $\sigma_{\text{exp}}^R(j) = \sigma_{\text{exp}}(j)(\bar\sigma/\bar\sigma_{\text{exp}})$ is the renormalized ex-

FIG. 13. Distribution of events in the decay angles (a) polar angle $\cos\theta$ and (b) azimuthal angle ϕ, for the final state $\mu^- p \pi^+$. The curves are the predictions of the Adler model.

TABLE VI. $\Delta^{++}(1236)$ density matrix elements.

Angular or q^2 range	$\tilde{\rho}_{33}$	$\tilde{\rho}_{31}$	$\tilde{\rho}_{3-1}$	Events
$-1.0 \leq \cos\theta^* \leq 1.0$	0.682 ± 0.056	-0.129 ± 0.063	-0.036 ± 0.068	317
$-1.0 \leq \cos\theta^* \leq 0.0$	0.638 ± 0.097	-0.056 ± 0.120	-0.166 ± 0.118	96
$0.0 \leq \cos\theta^* \leq 0.5$	0.685 ± 0.109	$+0.100 \pm 0.117$	-0.124 ± 0.128	96
$0.5 \leq \cos\theta^* \leq 1.0$	0.713 ± 0.087	-0.361 ± 0.092	$+0.131 \pm 0.109$	125
$0.0 \leq q^2 \leq 0.10$ $(\text{GeV}/c)^2$	0.634 ± 0.134	-0.400 ± 0.138	-0.122 ± 0.150	59
$0.10 \leq q^2 \leq 0.30$ $(\text{GeV}/c)^2$	0.679 ± 0.093	-0.124 ± 0.098	$+0.177 \pm 0.111$	121
$0.30 \leq q^2 \leq 0.60$ $(\text{GeV}/c)^2$	0.694 ± 0.100	$+0.035 \pm 0.123$	-0.132 ± 0.125	90

perimental cross section for energy bin j, and $\bar{\sigma}$ is the flux-averaged cross section.

Assuming Adler's model to hold, we may first determine the value of M_A. We find $M_A = 0.93 \pm 0.11$ GeV, in good agreement with our value of 0.95 ± 0.09 GeV from the direct measurement using the reaction $\nu n \to \mu^- p$.[1] The Adler model (with $M_A = 0.95$ GeV) is compared with our data in Figs. 3, 8, 10, 13, and 14. In general, good agreement is found, even with regard to such details as the q^2 dependence of the $\tilde{\rho}_{31}$ density matrix element.

However, since C_3^A and C_4^A are quite model-dependent and do not depend upon any firm theoretical basis (such as CVC and PCAC), we next want
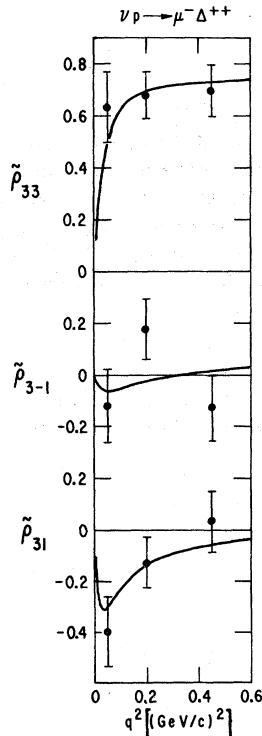

FIG. 14. Values of the density matrix elements $\tilde{\rho}_{mn}$ as a function of q^2 for the reaction $\nu p \to \mu^- \Delta^{++}$. The curves are the predictions of the Adler model with $M_A = 0.95$ GeV.

to explore the sensitivity of the fit with $C_3^A(0)$ and $C_4^A(0)$ as free parameters, the value of M_A fixed to be 0.95 GeV, and the q^2 dependence of C_3^A and C_4^A as parameterized by Adler. Figure 16 shows the resulting 1- and 3-standard-deviations limits on the two coupling-constant parameters. There is clearly a strong correlation between the two parameters, with $C_3^A \approx -C_4^A$ being favored. The predictions of Adler, shown as the box, agree well with this fit; Zucker's prediction, shown as the circle, is about 2 standard deviations away from the data. Any future model building will be highly restricted by these results.

Finally, we have tested the PCAC hypotheses by studying $d\sigma/dq^2$ near $q^2 = 0$. At $q^2 = 0$ (an unphysical value),[10] one has the simple expression

$$\frac{d\sigma}{dq^2} (q^2 = 0) = \frac{(\sqrt{3}G)^2}{12\pi} \left(\frac{s - W^2}{s - M^2}\right)\left(\frac{M + W}{M}\right)(C_5^A)^2 .$$

The contributions to the cross section from the other axial-vector form factors as q^2 increases make a test of the PCAC prediction ($C_5^A = 1.20$) difficult at large q^2. Figure 17(a) shows the overall q^2 distribution compared to Adler's prediction. The agreement is good. However, for $q^2 < 0.1$ $(\text{GeV}/c)^2$, the additional contributions are only weakly dependent upon the poorly known C_3^A and C_4^A form factors. This can be seen in Fig. 17(b), which shows the predictions for $d\sigma/dq^2$ for the various combinations of C_3^A, C_4^A, and C_5^A, given in the figure caption. It is clear that $d\sigma/dq^2$ near $q^2 = 0$ is a strong function of C_5^A and a weak function of

TABLE VII. Illegal Y_L^M moments for $\Delta^{++}(1236)$ decay.

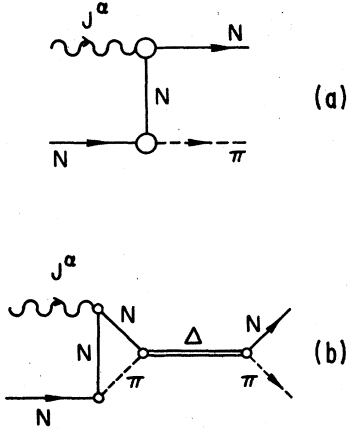| $\langle Y_L^M \rangle$		$\langle Y_L^M \rangle$	
Y_1^0	-0.027 ± 0.015	$\text{Re}Y_3^1$	-0.006 ± 0.010
$\text{Re}Y_1^1$	0.002 ± 0.012	$\text{Im}Y_3^1$	-0.008 ± 0.010
$\text{Im}Y_1^1$	0.007 ± 0.011	$\text{Re}Y_3^2$	0.007 ± 0.012
$\text{Im}Y_2^1$	-0.009 ± 0.011	$\text{Im}Y_3^2$	0.016 ± 0.011
$\text{Im}Y_2^2$	-0.011 ± 0.011	$\text{Re}Y_3^3$	0.002 ± 0.011
Y_3^0	0.029 ± 0.015	$\text{Im}Y_3^3$	-0.002 ± 0.012

FIG. 15. (a) Nucleon-exchange Born diagram. (b) Intermediate s-channel Δ rescattering diagram.

C_3^A and C_4^A if $|C_{3,4}^A| \lesssim C_5^A$, as suggested by Adler's detailed calculations.

The data plotted in Figs. 17(a) and 17(b) have the selections $0.5 \leqslant E_\nu \leqslant 6.0$ GeV and $M(p\pi^+) \leqslant 1.4$ GeV. We find good agreement with the PCAC prediction of $C_5^A = 1.2$ and conclude that PCAC is correct to an accuracy of about $\pm 20\%$.

C. Isospin analysis

The amplitudes for the production of the three pion-nucleon charge combinations in the final states $\mu^- p\pi^+$, $\mu^- p\pi^0$, and $\mu^- n\pi^+$ can be written as follows:

$$A(p\pi^+) = A_3 - (1/\sqrt{5})B_3, \tag{1}$$

$$A(p\pi^0) = (\sqrt{2}/3)A_3 - (\sqrt{2}/3)A_1 + (2/5)^{1/2}B_3, \tag{2}$$

$$A(n\pi^+) = \tfrac{1}{3}A_3 + \tfrac{2}{3}A_1 + (1/\sqrt{5})B_3, \tag{3}$$

where A_1 and A_3 are isovector exchange amplitudes and B_3 is a hypothetical isotensor exchange amplitude. The subscripts denote twice the isospin of the final hadronic state. One would like to measure the magnitude and phase of these amplitudes as a function of the $N\pi$ mass. Because of the limited data sample however, this goal can only be partially achieved.

To measure the A_1 and B_3 amplitudes, we must consider the $\mu^- p\pi^0$ and $\mu^- n\pi^+$ reactions in detail. The π-nucleon mass distributions for all three

single-pion production channels were presented in Fig. 3. After all the experimental corrections have been made and with the selection $M(N\pi) < 1.4$ GeV, we find $220.6 \pm 21 \mu^- p\pi^+$, $75.9 \pm 10.4 \mu^- p\pi^0$, and $60.1 \pm 9.0 \mu^- n\pi^+$ events in the deuterium film sample. We use this restricted sample in order to remove any flux-dependent corrections.

We now examine the isospin amplitudes given in Eqs. (1)–(3). If B_3 is zero, the amplitides $A(p\pi^+)$, $A(n\pi^+)$, and $A(p\pi^0)$ must satisfy a set of triangle inequalities. Moreover, if $B_3 \neq 0$, it is still possible with minimal assumptions to set an upper limit on $|B_3/A_3|$.

If $B_3 = A_1 = 0$, then we expect that

$$R^+ = \sigma(\mu^- n\pi^+)/\sigma(\mu^- p\pi^0) = \tfrac{1}{2}$$

and

$$R^{++} = [\sigma(\mu^- n\pi^+) + \sigma(\mu^- p\pi^0)]/\sigma(\mu^- p\pi^+) = \tfrac{1}{3}.$$

Our experimental results [for $M(N\pi) < 1.4$ GeV], $R^+ = 0.79 \pm 0.16$ and $R^{++} = 0.62 \pm 0.09$ imply the existence of at least an A_1 amplitude in addition to the A_3 amplitude. The Adler model predicts $R^+ = 0.77$ and $R^{++} = 0.58$, in agreement with these results. The model also agrees well with other aspects of the data as discussed in the previous section of the paper. In particular, it gives a reasonable representation of the $N\pi$ mass distributions of Fig. 3 and the excitation functions of Fig. 8.

If we assume that isotensor exchange is absent, i.e., $B_3 = 0$, we find that our data satisfy the resulting triangle inequalities. Consequently, isospin 2 exchange is not required by the data. Assuming that $B_3 = 0$, we can solve for the magnitudes of A_1 and A_3, as well as their relative phase η. For $M(N\pi) < 1.4$ GeV, we obtain $|A_1|/|A_3| = 0.65 \pm 0.08$ and $\eta = 95° \pm 9°$, which is consistent with a resonant $I = \tfrac{3}{2}$ amplitude in the presence of a large nonresonant $I = \tfrac{1}{2}$ $N\pi$ background.

If we allow B_3 to be nonzero, but require that it feed only the $\Delta(1236)$ resonance, as does A_3, then it must be real relative to A_3. One then finds the following relationship between the amplitudes:

$$\frac{(\sqrt{5} + 3\alpha)}{(\sqrt{5} - \alpha)} A(p\pi^+) = A(n\pi^+) + A(p\pi^0),$$

where $\alpha = B_3/A_3$. The resulting triangle inequal-

TABLE VIII. Parametrization of axial-vector form factors. $C_i^A(q^2) = C_i^A(0)[1 - aq^2/(b - q^2)]/(1 - q^2/M_A^2)^2$.

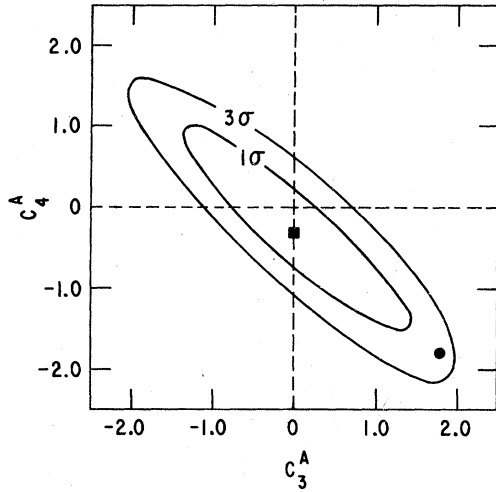|	$C_3^A(0)$	a	b	$C_4^A(0)$	a	b	$C_5^A(0)$	a	b
Adler	0			−0.3	−1.21	2.0	1.2	−1.21	2.0
Zucker	1.8	−1.11	0.63	−1.8	−1.05	0.77	1.9	−1.11	1.32

FIG. 16. 1- and 3-standard-deviation limits on C_3^A and C_4^A at $q^2 = 0$ as measured in the reaction $\nu p \rightarrow \mu^- \Delta^{++}$. The Adler and Zucker predictions are shown as the square and circle, respectively.
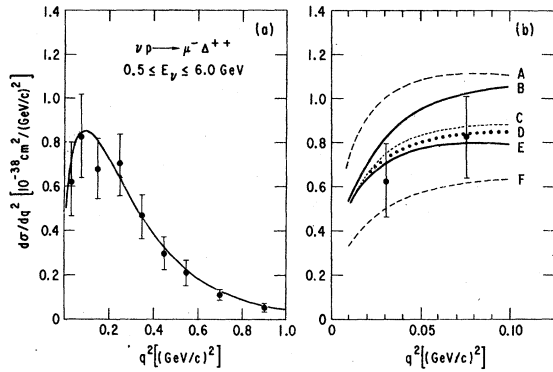

FIG. 17. (a) The differential cross section $d\sigma/dq^2$ for the reaction $\nu p \rightarrow \mu^- \Delta^{++}$ with the selections $0.5 < E_\nu < 6.0$ GeV and $M(p\pi^+) < 1.4$ GeV. The curve is the prediction of the Adler model with $M_A = 0.95$ GeV. (b) The differential cross section near $q^2 = 0$ for the reaction $\nu p \rightarrow \mu^- \Delta^{++}$. The curves are calculated for the following choice of parameters:

	$C_3^A(0)$	$C_4^A(0)$	$C_5^A(0)$
A	0	-0.3	1.44
B	$\begin{cases} 0 \\ 1.0 \end{cases}$	$\begin{cases} 1.0 \\ 0 \end{cases}$	$\begin{cases} 1.2 \\ 1.2 \end{cases}$
C	$\begin{cases} -1.0 \\ 1.0 \end{cases}$	$\begin{cases} 1.0 \\ -1.0 \end{cases}$	$\begin{cases} 1.2 \\ 1.2 \end{cases}$
D	0	-0.3	1.2
E	$\begin{cases} -1.0 \\ 0 \end{cases}$	$\begin{cases} 0 \\ -1.0 \end{cases}$	$\begin{cases} 1.2 \\ 1.2 \end{cases}$
F	0	-0.3	0.96

ities for the magnitudes are satisfied only if $-0.47 \pm 0.02 \leqslant B_3/A_3 \leqslant 0.12 \pm 0.04$.

D. Tests for the possible presence of second-class currents

Several recent nuclear-physics experiments have reported evidence for the existence of second-class axial-vector currents (SCC)[11] and the possibility of observing SCC in neutrino production of the $\Delta(1236)$ has been discussed. Holstein and Treiman[12] suggest that the $d\sigma/d\phi$ distribution for the Δ decay is quite sensitive to the presence of SCC. Pais[13] has shown that the most general form of the ϕ distribution consistent with present theoretical ideas is

$$\frac{d\sigma}{d\phi} = \sigma_0 + \sigma_1 \cos\phi + \sigma_2 \cos2\phi + \sigma_3 \sin\phi + \sigma_4 \sin2\phi.$$

In the Holstein-Treiman model, the σ_2 term would possibly be strongly modified by a SCC; the other σ_i's would also be modified but not to such a large degree. Figure 13 compares our ϕ distribution with the Adler model, which contains only the usual first-class currents. To the extent that the Adler model gives a good representation of the data, we see no evidence for the presence of SCC.

IV. STRANGE-PARTICLE PRODUCTION

Strange-particle production was observed in the following reactions:

$$\nu d \rightarrow \nu \Lambda K_S^0(p_s) \quad (\Lambda \rightarrow p\pi^-, \ K_S^0 \rightarrow \pi^+\pi^-),$$

$$\nu d \rightarrow \mu^- \Lambda K^+(p_s) \quad (\Lambda \rightarrow p\pi^-),$$

$$\nu d \rightarrow \mu^- \pi^+ \Lambda K_L^0(p_s) \quad (\Lambda \rightarrow p\pi^-, \ K_L^0 \rightarrow \pi^+\mu^-\bar\nu),$$

$$\nu d \rightarrow \mu^- K^+ \Lambda \pi^0(p_s) \quad (\Lambda \rightarrow p\pi^-),$$

$$\nu d \rightarrow \mu^- \pi^+ K_S^0 n(p_s) \quad (K_S^0 \rightarrow \pi^+\pi^-),$$

$$\nu d \rightarrow \mu^- pK^+K^0\pi^0(n_s) \quad (K^+ \rightarrow \mu^+\nu, \ K_S^0 \rightarrow \pi^+\pi^-),$$

$$\nu d \rightarrow \mu^- pK_S^0(p_s) \quad (K_S^0 \rightarrow \pi^+\pi^-).$$

$$\nu p \rightarrow \mu^- pK^+$$

This experiment is sensitive to K^0 and Λ production at all momenta by means of the $K_S^0 \rightarrow \pi^+\pi^-$ and $\Lambda \rightarrow p\pi^-$ decays. If an event contained a K_S^0 or Λ decay, all charged-particle tracks were carefully examined for particle mass identification using bubble density, the various decay modes, and secondary scatters. Pions can be separated from kaons using bubble density if the momentum is less than about 0.6 GeV/c. Although charged kaons can, in general, be identified by 3C kinematic fits at production, it was required that the kaon also be identified by visual means. Charged-Σ production was difficult to isolate in deuterium because there are many $\pi^\pm n \rightarrow \pi^\pm n$ and $pn \rightarrow pn$ secondary scatters.

TABLE IX. Properties of the strange-particle events.

Reaction	E_ν (GeV)	q^2 [(GeV/c)^2]	y	x	Hadronic mass (GeV)	Event number
$\nu n \to \nu \Lambda K^0$	2.05 ± 0.45	0.19	0.68	0.07	1.819	1
$\nu n \to \mu^- \Lambda K^+$	1.73 ± 0.02	0.10	0.73	0.04	1.824	2
	2.29 ± 0.02	0.42	0.62	0.16	1.753	3
	3.20 ± 0.02	1.36	0.54	0.42	1.623	4
$\nu n \to \mu^- \pi^+ \Lambda K^0$	5.81 ± 0.10	0.64	0.54	0.11	2.493	5
$\nu n \to \mu^- K^+ \Lambda \pi^0$	3.27 ± 0.06	1.59	0.90	0.29	2.095	6
$\nu n \to \mu^- \pi^+ K^0 n$	5.5 ± 0.3	0.23	0.49	0.46	1.888	7
$\nu p \to \mu^- p K^+ \bar{K}^0 \pi^0$	5.5 ± 0.4	2.72	0.91	0.29	2.748	8
$\nu n \to \mu^- p K^0$	1.59 ± 0.02	0.09	0.45	0.07	1.442	9
$\nu p \to \mu^- p K^+$	6.13 ± 0.13	0.21	0.12	0.15	1.445	10

$\Sigma^\pm$ production was searched for in the hydrogen film, and no events were found. In summary, all of our strange-particle events contain a K_S^0 or Λ decay, or are 3C kinematic fits at the production vertex. The scanning efficiency for the strange-particle reactions was $\geq 95\%$. The kinematic properties of the ten events found are given in Table IX. The associated production event, induced by the neutral current (event 1 of Table IX), has been discussed in detail in a previous publication.[14]

While we note that any background or ambiguities to the CC events are certainly negligible (except for the Λ/Σ^0 ambiguity), one must seriously consider the possibility that the zero-constraint event number 1 is really due to a neutron-induced process. This background has been calculated to be 0.021 ± 0.016 events based on the measured neutron flux and known cross sections.

Event 3 also fits the reaction $\nu d \to \mu^- \Lambda \pi^+(p_s)$. Because the π^+ has momentum 862 ± 11 MeV/c and leaves the chamber without any secondary interaction, we are not able to resolve directly the π^+/K^+ mass ambiguity. But since the kinematic χ^2 probability for $\mu^- \Lambda K^+$ is six times larger than that for $\mu^- \Lambda \pi^+$, we accept only the former hypotheses. We thus find no evidence for Λ production by means of the $\Delta S = -\Delta Q$ mechanism. Event 6 is ambiguous with the reactions $\nu d \to \mu^- \pi^+ \Lambda \pi^0(p_s)$ and $\nu d \to \mu^- K^+ \Lambda K^0(p_s)$. The $\mu^- K^+ \Lambda \pi^0$ final state was chosen for tabulation because it is not strangeness-changing and it yields a lower beam energy for the event. Event 7 is ambiguous with the reaction $\nu d \to \mu^- \pi^+ K_S^0 K^0 n(p_s)$. The $\mu^- \pi^+ K^0 n$ final state was chosen only because the event would then have a lower beam energy.

This experiment represents one of the few measurements of the rate of strange-particle production by the charged current. For $E_\nu \geq 1.5$ GeV, we measure

$$R^{sp} = \frac{\sigma(\nu d \to \mu^- + \text{strange particles})}{\sigma(\nu d \to \mu^- + \text{all})}$$

$$\geq 0.052 \pm 0.018 .$$

For hadronic masses in the range $1.4 \leq W \leq 3.0$ GeV, the results become

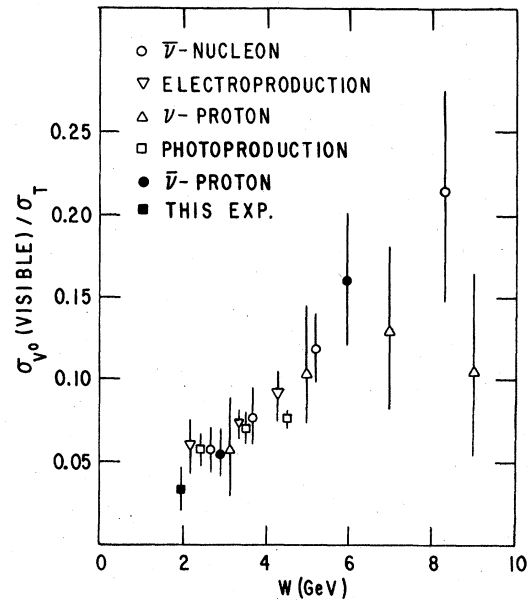$$R^{sp} \geq 0.075 \pm 0.027$$

FIG. 18. Rate of visible-strange-particle production as a function of hadronic mass W for various lepton- and photon-induced processes, as obtained from the following references: γp: A. J. Sadoff et al., Phys. Rev. Lett. **32**, 955 (1974); H. H. Bingham et al., Phys. Rev. D **8**, 127 (1973); μp: J. Ballam et al., Phys. Lett. **56B**, 193 (1975); νp: J. P. Berge et al., Phys. Rev. Lett. **36**, 127 (1976); $\bar{\nu} N$: F. A. Nezrick, SLAC Summer Institute talk, 1976 (unpublished).
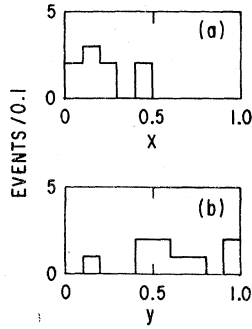
EVENTS / 0.1

FIG. 19. The distribution in (a) $x = q^2/2M(E_\nu - E_\mu)$ and (b) $y = (E_\nu - E_\mu)/E_\nu$ for the events with visible strange particles.

and

$$R^{sp}(\text{visible } V^0) = 0.034 \pm 0.013 .$$

The latter result is compared with measurements[15] using higher-energy neutrino beams as well as data from electroproduction and photoproduction experiments in Fig. 18.

Figures 19(a), 19(b) displays the $x = q^2/2M(E_\nu - E_\mu)$ and $y = (E_\nu - E_\mu)/E_\nu$ distributions of the strange-particle events. The strange-particle events tend to populate the larger-y and smaller-x values when compared to the inclusive sample of data.

Finally, we note that the two events of single-K-meson production (events 9 and 10) occur at the small values of x expected since they can only come from the quark/antiquark sea.

V. EVENTS OF THE FOUR- AND FIVE-PRONG TOPOLOGY

There are 44 neutrino-induced events in the experiment with four or five charged particles in the final state. These events are classified as belonging to the final states listed in Table I as follows: (4) $(\mu^- p \pi^+ \pi^+ \pi^-)$, (5) $\mu^- p \pi^+ \pi^+ \pi^- \pi^0$, (6) $\mu^- n \pi^+ \pi^+ \pi^+ \pi^-$, (13) $\mu^- p \pi^+ \pi^-$, (14) $[\mu^- p \pi^+ \pi^- (l\pi^0), l \geq 1]$, and (15) $[\mu^- n \pi^+ \pi^+ \pi^- (m\pi^0), m \geq 0]$. As was done for the $\mu^- p$ and $\mu^- p \pi^+$ final states, three-constraint kinematic fits were performed in order to isolate the events of reactions (4) and (13). Events with χ^2 probability less than 1% for the 3C fits were classified as belonging to reactions [(15) or (14)] or [(6) or (5)] depending on the presence or absence of an identified proton in the final state. In all cases, we assumed only a single neutral particle was produced in the event.

After kinematic fitting, there are two types of ambiguities which can occur. First, there is a μ^-/π^- mass ambiguity whenever the two negative tracks both leave the chamber without undergoing a strong interaction in the liquid. This ambiguity

exists in 30% of the events. By examining the unique four- and five-prong events (those where a π^- scatters or decays, or where the μ^- decays), it was decided to resolve the μ^-/π^- ambiguity as follows: If the faster negative track has momentum greater than 0.5 GeV/c and the ratio P_{fast}/P_{slow} of the faster-to-slower negative tracks is greater than 1.5, then the faster track is classified as the muon. For the three ambiguous events not resolved by this rule, the hypothesis with the smaller total hadronic mass was chosen. Based on the unique events, it is estimated that 2 ± 1 events have been misclassified using these techniques.

The second type of ambiguity, present in 20% of the four- and five-prong events, is the π^+/proton mass ambiguity. This condition can exist whenever two positive tracks have momentum greater than 1.0 GeV/c so that ionization information is not available. Based upon the unique events of reactions (4)–(6) and (13)–(16) and the properties of the $\nu p \to \mu^- p \pi^+$ events, the ambiguity was resolved by choosing the faster positive track as the nucleon. The estimated error in the resulting track classifications is 1 ± 1 events. The numbers of events assigned to the various reactions are given in Ta-
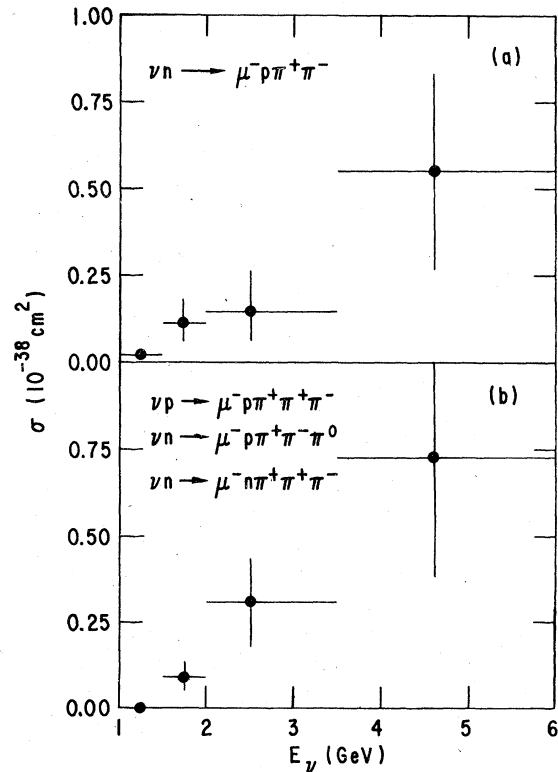
σ (10^{-38} cm^2)

E_ν (GeV)

FIG. 20. Excitation functions for (a) the double-pion production reaction $\nu n \to \mu^- p \pi^+ \pi^-$, (b) the sum of the three triple-pion production reactions, $\nu p \to \mu^- p \pi^+ \pi^+ \pi^-$, $\nu n \to \mu^- p \pi^+ \pi^- \pi^0$, and $\nu n \to \mu^- n \pi^+ \pi^+ \pi^-$.
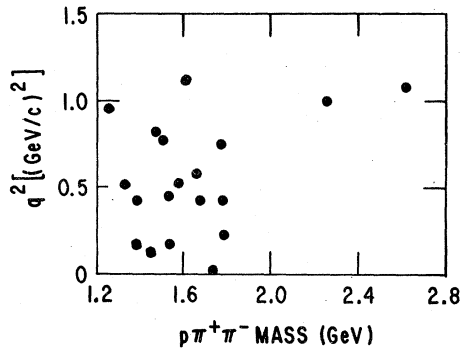
FIG. 21. Scatter plot of q^2 versus $p\pi^+\pi^-$ mass for events of the reaction $\nu n \to \mu^- \bar{p}\pi^+\pi^-$.

ble I.

The excitation functions for $\nu n \to \mu^- \bar{p}\pi^+\pi^-$ and for the *sum* of the three-pion production reactions $\nu p \to \mu^- \bar{p}\pi^+\pi^+\pi^-$, $\nu n \to \mu^- \bar{p}\pi^+\pi^-\pi^0$, and $\nu n \to \mu^- \bar{n}\pi^+\pi^+\pi^-$ are shown in Fig. 20. The cross sections rise quickly from threshold, and for E_ν in the range 3.5–6.0 GeV are about equal to the cross sections for the $\nu n \to \mu^- \bar{p}$ and $\nu p \to \mu^- \bar{p}\pi^+$ reactions.

Only the $\nu n \to \mu^- \bar{p}\pi^+\pi^-$ data sample is large enough to permit a study of the production dynamics. Figure 21 shows the correlation between q^2 and
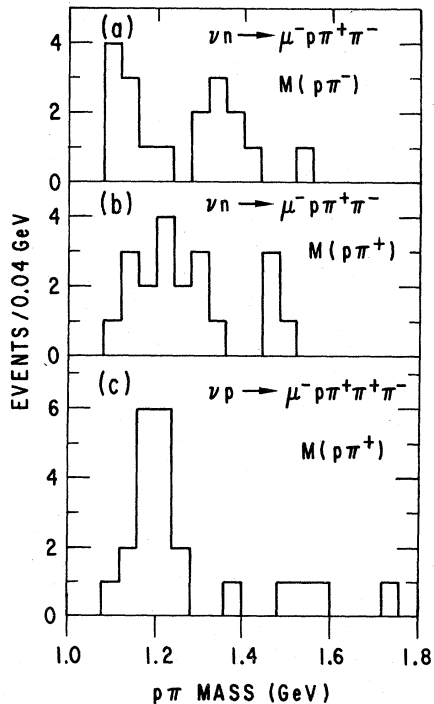

FIG. 22. $N\pi$ mass distributions for the constrained four- and five-prong events (a) $M(p\pi^-)$ for events of the reaction $\nu n \to \mu^- \bar{p}\pi^+\pi^-$, (b) $M(p\pi^+)$ for the events of the reaction $\nu n \to \mu^- \bar{p}\pi^+\pi^-$, and (c) $M(p\pi^+)$ for the events of the reaction $\nu p \to \mu^- \bar{p}\pi^+\pi^+\pi^-$.

the $p\pi^+\pi^-$ invariant mass. Most of the events have low q^2, but there is no apparent structure in the mass spectrum. Figures 22(a)–22(b) show the $p\pi^-$ and $p\pi^+$ mass distributions; some evidence for $\Delta^{++}(1236)$ production is apparent. The $\pi^+\pi^-$ mass spectrum (not shown) gives no evidence for $\rho^0(760)$ production.

The events of reaction (4) also show a clear Δ^{++} signal as seen in Fig. 22(c), but no other resonance production in reactions (4)–(6) and (13)–(15) is evident in any of the multipion production events at our present low statistical level.

VI. MULTINEUTRAL FINAL STATES

A. Kinematics

We have discussed the analysis of the events with four or more charged prongs in the previous section. For that data sample, the unconstrained events were assigned a single neutral particle either, π^0 or neutron. This technique can be used because of the low pion multiplicity observed with the flux of this experiment. We now describe the method used to separate events of the two and three-prong topologies with one neutral particle from those having more than one missing neutral. The approach is statistical, relying upon the 3C fits in the final states with single and multiple pions, and the assumption that the kinematical distributions are similar for the mixed charged-neutral and for the completely charged final states. The method described permits us to separate the multipion background from the single-pion final states $\mu^- p\pi^0$ and $\mu^- n\pi^+$ at incident neutrino energies above 1.5 GeV and thus is complementary to the analysis given in Sec. II B.

Events of interest with multiple missing neutrals are categorized into the reactions listed in Table I as follows: (2) $[\mu^- p\pi^+(l\pi^0), \ l \ge 1]$, (3) $[\mu^- n\pi^+\pi^+(m\pi^0), \ m \ge 0]$, (11) $[\mu^- p(k\pi^0), \ k \ge 2]$, and (12) $[\mu^- n\pi^+(l\pi^0), \ l \ge 1]$. Each of these events appears as either a two-prong [reactions (11) and (12) with an unseen spectator], or a three-prong topology. In the deuterium portion of the data, events of reactions (2) and (3) also have unseen neutron spectators. Because these final states are underconstrained, the incident neutrino energy cannot be directly computed from the observed particle momenta.

In order to describe the kinematics of the underconstrained events, we note that the incident projectile is massless, and thus there is a linear relation between the incident-beam energy and the mass-squared of the missing neutral system:

$$M_0^2 = C + DE_\nu. \tag{4}$$

The quantities C and D are computable for each event in terms of the observed particle momenta

and masses and are given by

$$C = \left(M - \sum E_i\right)^2 - \left(\sum P_i\right)^2 \qquad (5)$$

$$D = 2\left(M - \sum E_i + \sum P_{iv}\right), \qquad (6)$$

where M is the target mass, the summations are over all the observed tracks (including the spectator for deuterium events), and P_{iv} is the component of momentum along the incident neutrino direction. The quantity C is the four-momentum between the neutrino and the neutral system, whereas D is related to the transverse momentum of the neutral system as can be derived from (6):

$$D = 2(E_0 - P_{0v}) \approx 2P_{T0} + \frac{M_0^2}{P_0} + \cdots .$$

Three rules follow immediately from these relations for the true neutrino-induced events: (a) C and D are correlated by Eq. (4), (b) for events with no missing neutrals, $M_0^2 = 0$ and $C = D = 0$, and (c) $D \geqslant 0$. Finally, we note from Eq. (4) that if a scatter plot is made of D versus C, lines of constant E_v radiate into the upper half of the plot originating from the point of the C axis equal to M_0^2 for each event. Of course, M_0^2 is only single valued for the reactions with a single missing neutral.

B. Selection criteria

All two- and three-prong events which did not give an acceptable fit to the $\mu^- p \pi^+(n_s)$ or $\mu^- p(p_s)$ final states were used in the analysis. Assuming the negative track to be a muon, the other tracks were assigned the pion and proton masses in turn unless the particle was identified by ionization, scattering, stopping information, or helix fit residuals. As an illustration, we show in Figs. 23(a) and 24(a) the C-D scatter plots for two-prong events, and three-prong events with a visible spectator. In Figs. 23 and 24, the final state is assumed to be $\mu^- p X^0$ or $\mu^- \pi^+ X^0$, respectively. When the fast positive track could not be identified, the event appears on both plots. In Fig. 23(a), a large clustering of events appears in the unphysical region having $D < 0$. These events correspond to incident low-momentum protons that scatter in the liquid.

In Fig. 24(a) we see a band of events extending from the unphysical into the physical region. The events in this band result from incident charged pions that scatter or decay, thus faking a two- or three-prong neutrino event. As the observed momenta nearly balance,
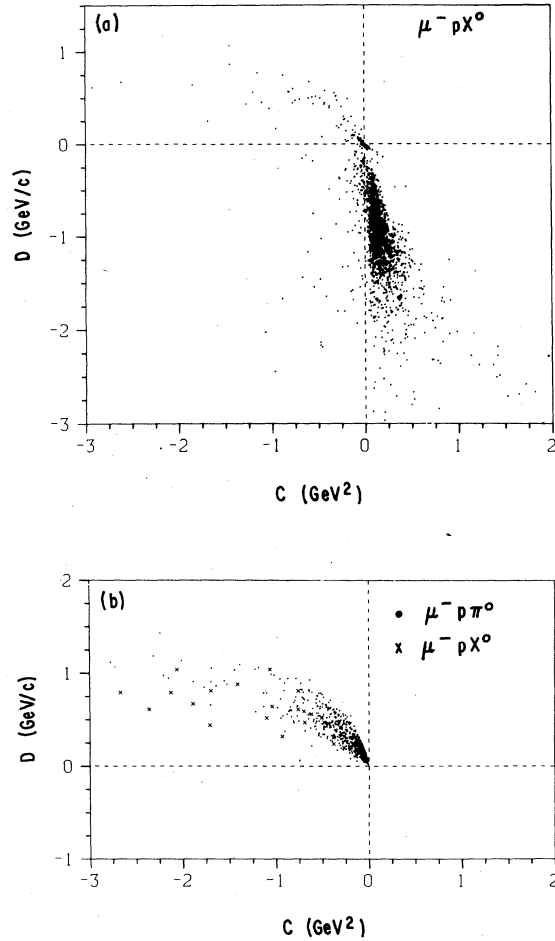
$$\sum P_i \approx 0,$$

FIG. 23. Distribution in the variables C and D (defined in the text). (a) All two-prong events of the final-state $\mu^- p X^0$ (plus three-prong events with a spectator proton). The large clustering of events with $D < 0$ corresponds to background from the incident hadrons that scatter in the liquid. (b) Predicted distributions for events of the $\mu^- p \pi^0$ final state shown as dots and events of multiple neutral-pion production $\mu^- p(k\pi^0)$, $k \geqslant 2$ shown as crosses. The distributions for the single-pion final states are calculated from the Adler model whereas for the multiple-pion production data, we use the multipronged events.

and so

$$C \simeq D^2/4 .$$

The dark band in Fig. 24(a) clearly follows this relation, confirming these events to be mostly background. The clustering of background events in Figs. 23(a) and 24(a) occurs because of the low momenta of the incident hadrons, predominantly <1 GeV/c. Applying the selection $D > 0$ eliminates most of the background in the proton case while leaving the signal unchanged.
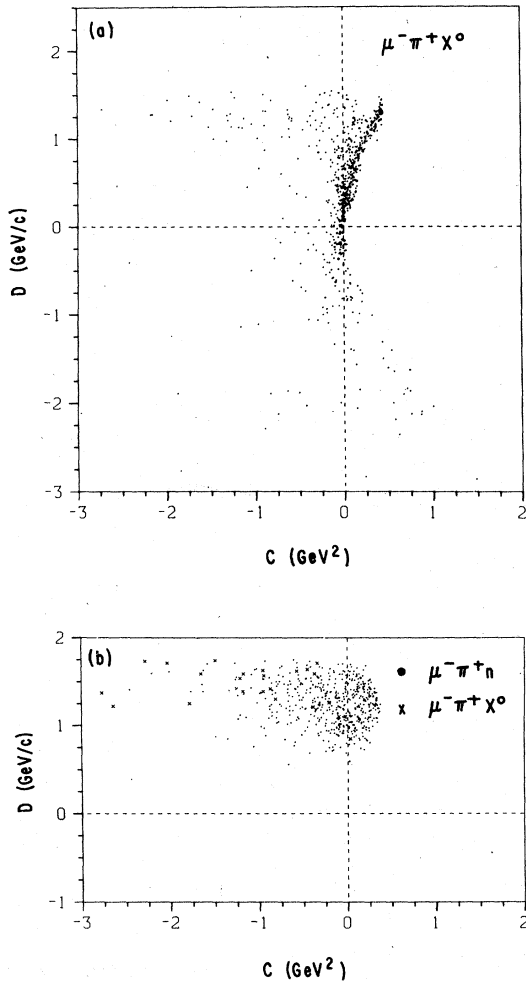
FIG. 24. Distribution in the variables C and D (defined in the text). (a) All two-prong events of the final-state $\mu^-\pi^+X^0$ (plus three-prong events with a spectator proton). (b) Predicted distributions for events of the $\mu^-n\pi^+$ final state shown as dots and events of the type $\mu^-n\pi^+ (l\pi^0)$, $l \geq =$ shown as crosses. The distributions for the single-pion final state are calculated from the Adler model, whereas for the multiple-pion production data, we use the multipronged events.

In order to eliminate the background in the π^+ sample, a set of colinearity cuts were applied to the data similar to those described in Sec. II B. However, whereas previously these cuts were applied to all the data, they are now applied only to the events within the band shown in Fig. 24(a). Using the constrained sample of multicharge pronged events [reactions (4) to (6) and (13) to (15) of Table I] and applying the same cuts, we estimate that no loss of real events occurs for the multineutral final states. However, a correction of 5.5% was necessary for the $\mu^-n\pi^+$ channel.

Each event in the physical region satisfying the

above cuts was examined on the scan table to check consistency and search for neutron scatters and γ rays. Protons with momenta less than 350 MeV/c were classified as spectators. In this way, mass interpretations were unambiguously assigned to 88% of the events. The ambiguous events were weighted equally into each appropriate final state consistent with the various mass assignments for each track. The three-pronged events (without a proton spectator) were analyzed in a similar way. For this sample, the background was relatively less important.

We have now selected the sample of neutrino-induced events and assigned the positive track to be either a proton or π^+. In order to isolate the single π^0 from the multi-π^0 final states, we again rely on the constrained multicharged data. By dropping appropriate combinations of tracks, these final states could be used to simulate the unconstrained reactions. In Figs. 23(b) and 24(b), we show the resulting C-D values for these simulated events as crosses. The single-pion final states $\mu^-p\pi^0$ and $\mu^-n\pi^+$ were simulated in two ways: (a) using the constrained $\mu^-p\pi^+n_s$ events, and (b) using Adler's model as discussed in Sec. II C for hadronic masses up to 1.4 GeV and phase space for higher masses. The resulting distributions were not noticeably different, so we decided to use method (b). The C-D distributions for these simulated events are also shown in Figs. 23(b) and 24(b) as dots.

The $\mu^-p\pi^0$ events separate well from the μ^-pX^0 events, the latter populating a region with $C < -0.3$ GeV^2. This separation can be related to the threshold behavior observed in the multipion cross section. On the other hand, the $\mu^-\pi^+n$ and $\mu^-\pi^+X^0$ final states appear to have a larger overlap because of the large missing masses present.

Assuming that the kinematics of the data are similar to the simulation, we have made a statistical separation. The C-D plots were divided into bins, and weights were assigned to each event based on the probability that it belonged to the single-neutral or multineutral final state.

An estimate was made of the background in each channel resulting from events induced by incident neutrons. Using the reaction $np \rightarrow pp\pi^-$ to normalize the neutron flux, a total of eight background events were estimated. Misidentified neutral-current events contribute less than one background event. After subtracting the background and correcting for scanning inefficiency, losses due to cuts, unmeasurable events, and the q^2 loss described in Sec. II B for the $\mu^-p\pi^0$ final state, the final number of events is shown in Table I.

No attempt was made to separate the single-neutral from multineutral events in reactions (2)

TABLE X. Errors on assigning the neutrino energy.

Final state [a]	$\langle P_{sv}\rangle$ (GeV/c)	$\langle\sum P_i\rangle$ (GeV/c)	$\langle D\rangle$ (GeV)	ΔC (GeV^2)	ΔD (GeV)	$\left(\dfrac{\delta P}{P_\nu}\right)_{sp}$ [c]	$\left(\dfrac{\delta P}{P_\nu}\right)_E$ [d]	$\left(\dfrac{\delta P}{P_\nu}\right)_{Total}$
$\mu^-\pi^+p(n_s)$ [b]	0.1	0.7	0	±0.07	±0.1			
$\mu^-\pi^+p(n_s)+X^0$	0.06	1.8	0.4	±1.03	±0.06	0.20	0.26	0.33
$\mu^-\pi^+\pi^-(n_s)+X^0$	0.06	1.1	1.0	±0.063	±0.06	0.08	0.23	0.24
$\mu^-\pi^+n(p_s)$	0.05	0.8	1.2	±0.04	±0.05	0.06	0.05	0.08
$\mu^-\pi^+n(p_s)+X^0$	0.05	1.0	1.48	±0.05	±0.05	0.05	0.22	0.23
$\mu^-\pi^0p(p_s)$	0.05	1.2	0.36	±0.06	±0.05	0.20	0.05	0.21
$\mu^-p(p_s)+X^0$	0.05	1.5	0.52	±0.075	±0.05	0.14	0.12	0.18

[a] Spectators are unseen because they are neutrons or protons with momentum $\lesssim 110$ MeV/c.

[b] Only for events not giving 3C fit, i.e., $P_{sp}\gtrsim 140$ MeV/c.

[c] Error due to assigning zero momentum to an unseen spectator (zero if spectator seen).

[d] Errors in assigning the neutrino energy either by 0C fit for single missing neutral or multicharge simulation in multineutral case.

and (3) due to the small number of multineutral events. However, as described in Sec. II A, reaction (2) has a background contribution from $\mu^-p\pi^+$ events in deuterium where the neutron spectator has large momentum. Because the true 3C fits will populate near the origin on the C-D plots and be spread out due to the missing spectator momentum, a cut of $C < -0.21$ GeV^2 was applied to remove these $\mu^-p\pi^+n_s$ background events. This cut was tested using the μ^-pp_s fitted events and was found to eliminate all of the background; a corresponding correction factor of 1.10 was necessary for the $\mu^-p\pi^+1\pi^0$ events effected by the cut. The corrected numbers of events are summarized in Table I.

C. Neutrino-energy assignment

The neutrino energy was assigned to each multineutral event using the C and D values for that event and the correlation of neutrino energy with these variables. The mass of the neutral system was parametrized using the form

$$M_0^2 = \alpha + \beta C + \gamma D + \delta CD. \tag{7}$$

After dropping the appropriate tracks from the constrained multiprong events, a fit was performed for each multineutral channel to Eq. (7) where M_0^2 is now a known quantity since we know the vector momenta of the discarded tracks. Using the fitted constants in (7), each multineutral event was assigned a M_0^2 value and, therefore, an E_ν according to its measured C and D values. The estimated percent errors on determining E_ν with this method are given for each final state in Table X, denoted as $(\delta P/P_\nu)_E$.

Also contributing to the error in assigning E_ν is the effect of an unseen spectator. The magnitude of this effect can be shown to be

$$\Delta C = C_{\text{real}} - C_{\text{meas}} \cong -P_S \sum P_j ,$$

$$\Delta D = D_{\text{real}} - D_{\text{meas}} \cong P_{Sv} ,$$

where P_S refers to the spectator. $\sum P_j$ will be roughly in the ν direction, therefore the equations become

$$\Delta C \approx -P_{Sv}\left|\sum P_j\right| , \tag{8}$$

$$\Delta D = P_{Sv}. \tag{9}$$

The effect of the unseen spectator will appear then on the C-D plot along a line of negative slope intercepting the origin. We illustrate this behavior coming from the unseen spectators in Fig. 25, where we plot C against D for the fitted events of the $\mu^-p\pi^+n_s$ final state that has an unseen neutron spectator. There is a clear linear relationship as predicted by (8) and (9). In Table X, we give an estimate of this source of error as $(\delta P_\nu/P_\nu)_{sp}$.
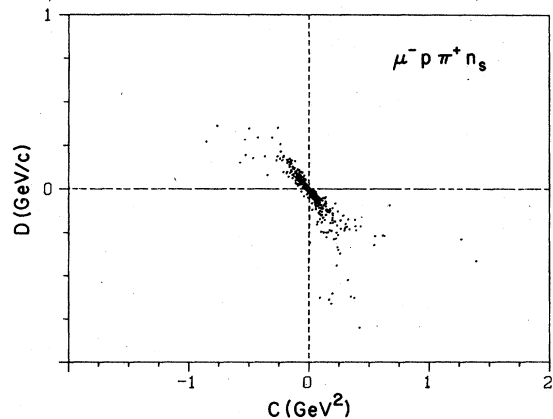

FIG. 25. Distribution in the variables C and D (defined in the text) for fitted events of the $\mu^-p\pi^+n_s$ final state. The measured track quantities are used in the calculation and the distribution along a line through the origin is a result of the unmeasured spectator momentum.
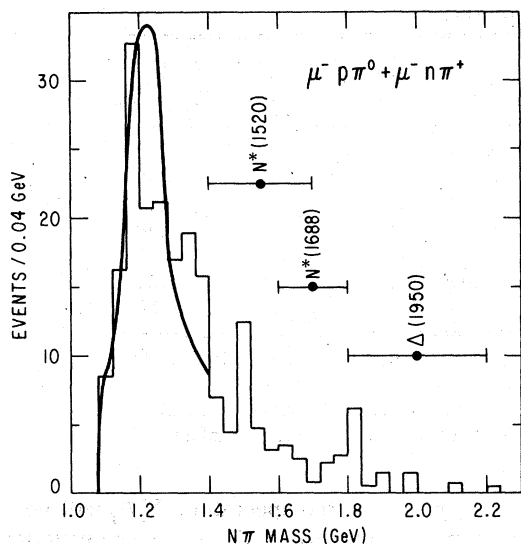
FIG. 26. Distribution in the $N\pi$ mass for the sum of the events in the final states $\mu^-p\pi^0$ and $\mu^-n\,\pi^+$ separated as described in the text. The distribution extends above the Δ region, perhaps reflecting the production of high-mass $T=\frac{1}{2}$ isobars. The curve is a prediction of the Adler model.

D. Hadronic mass distributions

First we compare our results for $\nu n \rightarrow \mu^- N\pi$ with those presented in Sec. II, which were obtained using a quite different analysis. The $N\pi$ mass plot
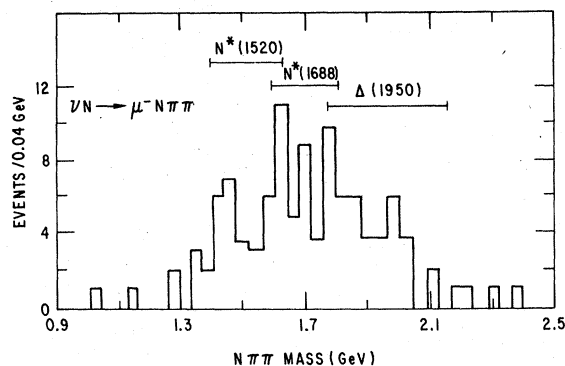

FIG. 27. Distribution in $N\pi\pi$ mass combining all data from the final states $\mu^-p\pi^+\pi^-$, $\mu^-p\pi^0\pi^0$, $\mu^-n\,\pi^+\pi^0$, $\mu^-p\pi^+\pi^0$, and $\mu^-n\,\pi^+\pi^+$.

appears in Fig. 26 with the curve given by the Adler model. This plot is consistent with the data presented in Sec. II and in Fig. 3 except now the distribution extends to somewhat higher masses. Making a cut at $M(N\pi)=1.4$ GeV, we obtain the same results for R^+ and R^{++} within the errors previously quoted.

Combining the charged-multipion sample discussed in the previous section with the multineutral sample, we have searched for evidence of higher N^* and Δ resonances. The $N^*(1525)$, $N^*(1688)$, and $\Delta(1950)$ have been predicted to be present by Zucker,[7] and they should appear in $N\pi$, $N\pi\pi$, and $\Delta\pi$ final states. In Figs. 26 and 27, we
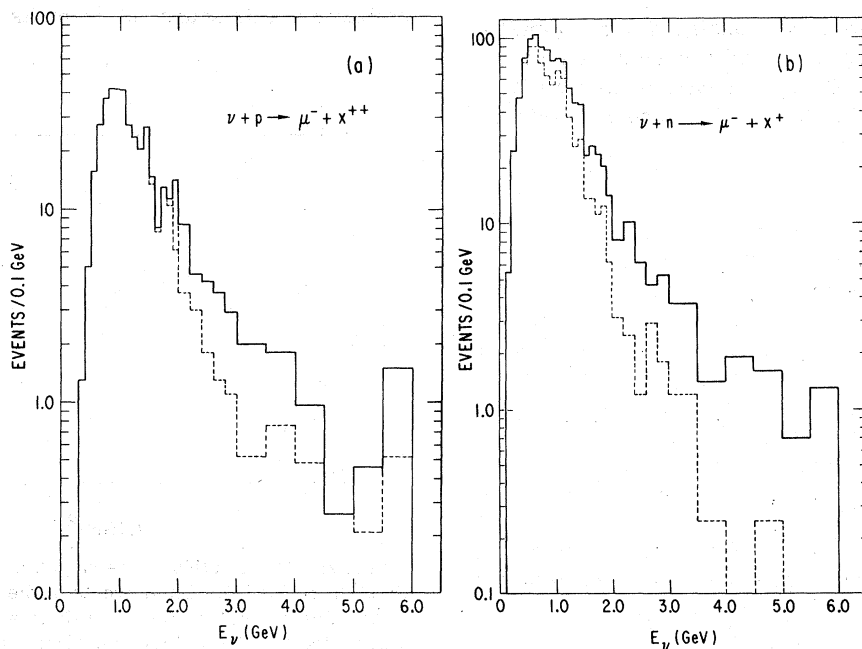

FIG. 28. Distribution of events in neutrino energy E_ν for (a) the reaction $\nu p \rightarrow \mu^- X^{++}$, and (b) the reaction $\nu n \rightarrow \mu^- X^+$. The dashed hisotgrams correspond to dominant $\mu^-p\pi^+$ and μ^-p final states, respectively.

show the total single-pion and double-pion mass plots where we have placed all events of the type $\mu^- p X^0$ and $\mu^- \pi^+ X^0$ into the double-pion distribution. There is no clear evidence for any higher-mass resonances, though there is an accumulation of events in the 1700-MeV mass region. The next higher Δ resonance predicted by Zucker is at 1950 MeV, and with his cross-section prediction we expect only a total of three events in the $N\pi$ mass plot.

Assuming that all events with hadronic masses from 1350 to 1850 MeV are due to $N^*(1525)$ and $N^*(1688)$ production in both the single- and double-pion mass plots, the integrated cross sections and

branching ratios are consistent with Zucker's prediction.

VII. PROPERTIES OF THE INCLUSIVE DISTRIBUTIONS

Data from lepton-nucleon scattering experiments, when compared to recent predictions of asymptotically free gauge theories (AFGT), show that the concept of scaling in the nucleon structure functions can be extended to low energies without defining new variables.[16] The change of the distributions with q^2 over a wide energy range is explained by scaling violations of the $\ln q^2$ type. Specifically, it has been shown that the energy dependence of the neutrino-nucleon x distribution can be represented by the expression[16]

$$\frac{dN}{dx}(x, E) \propto \frac{F_2(x, q_0^2)}{1 + f(x)} \left(\frac{2MEx}{q_0^2}\right)^{f(x)}, \qquad (10)$$

where $f(x) = 0.25 - x$.

At very low energies, only one or two exclusive channels are kinematically allowed and so these ideas should not apply. Our data extend from this threshold region into the kinematic regime where the scaling ideas are valid. In this section of the paper, we investigate this approach to the scaling region and, in addition, compare our data with re-
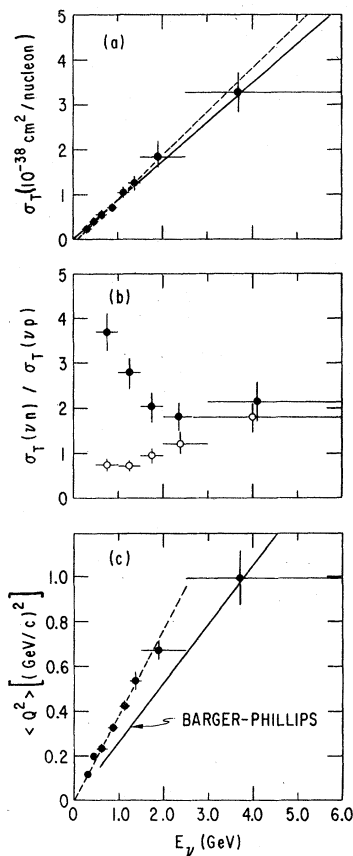

FIG. 29. (a) The total νN cross section, defined as half of $\sigma(\nu d)$, as a function of neutrino energy E_ν. The full line represents a linear fit through the origin, whereas the dashed line is the best linear fit without this constraint. (b) The ratio of the νn to νp cross sections as a function of neutrino energy. The filled circles correspond to all channels, whereas for the open circles, the quasi-elastic events have been removed. (c) Mean four-momentum transfer squared $\langle Q^2 \rangle$ as a function of neutrino energy. The dotted curve represents $\langle Q^2 \rangle = -0.01 + 0.35 E_\nu$; the solid curve is a typical QPM prediction.
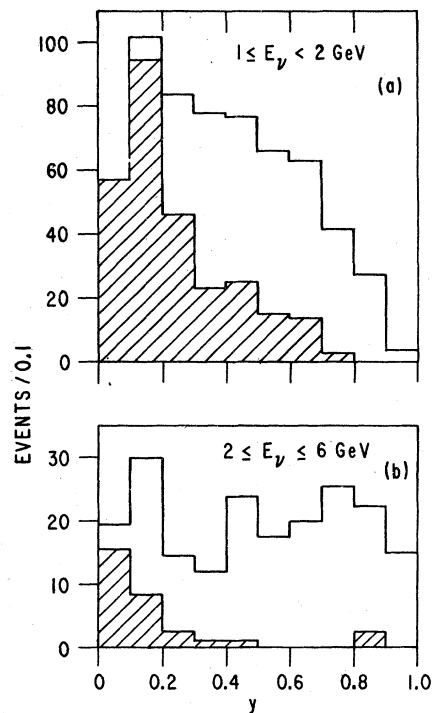

FIG. 30. The distribution in the variable $y = (E_\nu - E_\mu)/E_\nu$ for νd interactions with the energy selections (a) $1 < E_\nu < 2$ GeV, and (b) $2 < E_\nu < 6$ GeV. The quasi-elastic events are shown shaded.

sults from the high-energy experiments.

Figures 28(a), 28(b) shows the distribution of events in neutrino energy separately for neutron and proton targets. The reactions are, of course, dominated by the quasielastic ($\mu^- p$) and single-pion production ($\mu^- p\pi^+$) final states, respectively, as shown by the dashed histograms. The νN total cross section, defined as the mean of the νn and νp cross sections, is given in Fig. 29(a). The errors include a systematic flux uncertainty of $\pm 10\%$ folded in with the statistical error. Within errors, the cross section rises linearly with E_ν almost from theshold. A linear fit yields $\sigma_T(\nu N) = [(-0.07 \pm 0.05) + (0.96 \pm 0.06)] \times 10^{-38} E_\nu$ cm^2/nucleon GeV. With the constraint that $\sigma_T = 0$ at $E_\nu = 0$, one has $\sigma_T(\nu N) = (0.87 \pm 0.03) \times 10^{-38} E_\nu$ cm^2/nucleon GeV with $\chi^2/\mathrm{DF} = 4.4/7$. The only other νN cross-section measurement in this energy range is from a freon target in Gargamelle.[17] That experiment measured a slope of 0.81 ± 0.03 in the energy range 1–18 GeV. The results of the two experiments agree, although the final result of each experiment has changed somewhat from those initially published.[18]

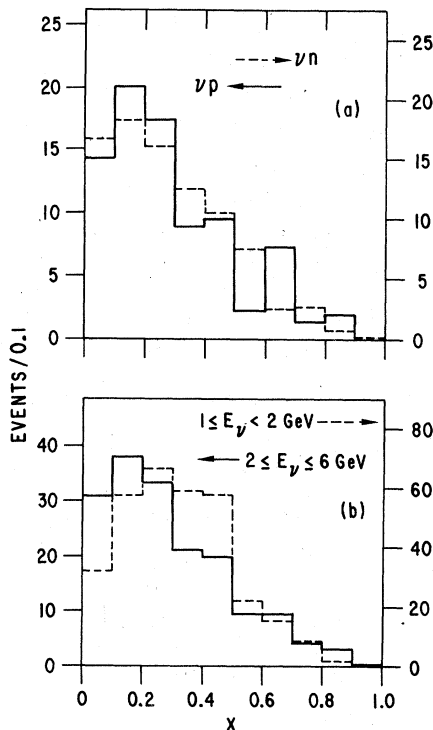Since the neutron has two down quarks and the proton only one, the simple quark model predicts

that the total-cross-section ration $R = \sigma_T(\nu n)/\sigma_T(\nu p)$ should be 2.0 if only the three valence quarks contribute. Recent specific scaling fits to electron, muon, and high-energy ν data predict a value of 1.95 ± 0.03.[19] Our measured cross-section ratio is shown in Fig. 29(b) as a function of E_ν. The open circles show the ratio with the quasielastic events removed. We use only the deuterium data in this plot so the measurement is independent of the flux. After a strong fall at low energies, where the quasielastic events dominate, the ratio levels off at about 2. For $E_\nu > 1.5$ GeV, we measure $R = 1.95 \pm 0.21$ for all the data and 1.12 ± 0.13, rising with increasing energy, if the quasielastic events are removed. Our results show that the scaling value is approached quickly.

Another check on the approach to scaling can be made by looking at the mean squared four-momentum transfer between the leptons, $\langle q^2 \rangle$, as a function of E_ν. As seen in Fig. 29(c), $\langle q^2 \rangle$ rises with E_ν and, using all the data, the best linear fit is $\langle q^2 \rangle = (-0.01 \pm 0.04) + (0.35 \pm 0.02)E_\nu$ with $\langle q^2 \rangle$ in (GeV/c)^2 and E_ν in GeV, as shown by the dotted line in Fig. 29(c). The fit is not good ($\chi^2/\mathrm{DF} = 15.2/6$). Restricting the fit to the events with $E_\nu > 1.0$ GeV gives $\langle q^2 \rangle = (0.16 \pm 0.08) + (0.25 \pm 0.04)E_\nu$ with $\chi^2/\mathrm{DF} = 2.5/2$. The fit is in agreement with that obtained

FIG. 31. The distributions in the variable $x = q^2/2M(E_\nu - E_\mu)$ (a) comparison of the νp (full histogram) and νn (dashed histogram) distributions for the energy selection $2 < E_\nu < 6$ GeV. (a) Comparison of the νd distribution for the two energy selections $1 < E_\nu < 2$ GeV (dashed histogram) and $2 < E_\nu < 6$ GeV (full histogram).
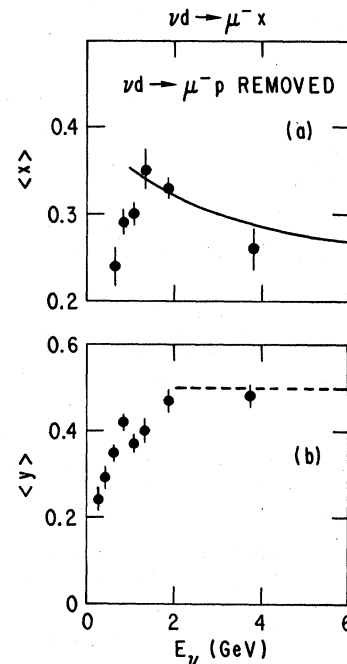

FIG. 32. Mean values of the scaling variables x and y as a function of neutrino energy. In both cases, there is a rapid rise to the scaling values. The full line in (a) shows the expected change of $\langle x \rangle$ with E_ν because of scaling breaking. The dotted line at $\langle y \rangle = 0.5$ corresponds to the mean value for a flat y distribution.

in the Gargamelle experiment[18] where $\langle q^2 \rangle$ = $(0.12 \pm 0.03) + (0.23 \pm 0.01)E_\nu$ represented the data with $E_\nu > 1$ GeV. The finite intercept presumably arises from the ν energy thresholds for the quasi-elastic and single-pion production channels. The solid curve shows the prediction of a typical QPM calculation.

The distributions in the scaling variable y are shown in Fig. 30 for νd interactions and the energy selections (a) $1 < E_\nu < 2$ GeV and (b) $2 < E_\nu < 6$ GeV. The y distribution is somewhat different in the two energy ranges, and is flatter for the high-energy selection in agreement with the expected scaling distribution. The contribution from the quasielastic channel $\nu n \rightarrow \mu^- p$ is shown shaded. In a low-energy experiment, the kinematical restrictions on y are important and favor the central y range.

The distributions in the other scaling variable are shown in Fig. 31. In this case since the quasi-elastic events have a singular distribution peaked at $x = 1$, we do not include them in the plots. In Fig. 31(a) we show the x distribution for the $2 < E_\nu < 6$ GeV selection separately for n and p targets. The distributions agree well, so that at the present statistical level, our results do not show evidence for a leading quark in the nucleon. The x distribution for νd interactions with the two energy selections $1 < E_\nu < 2$ GeV and $2 < E_\nu < 6$ GeV is shown in Fig. 31(b). The x distribution is narrower for the higher-energy selection.

The average values of x and y as a function of energy are shown in Fig. 32. For the distribution in $\langle x \rangle$, there is a rapid rise from threshold followed by a slow fall. The curve in Fig. 32(a) shows the x distribution from $eN \rightarrow eX$ inelastic scattering at $q^2 = 3.0$ $(\text{GeV}/c)^2$ modified using Eq. (10) appropriately for the 2–6 GeV neutrino-energy range of our data. The agreement for the higher-energy data is good when this form of scale violation is used. For the y distribution of Fig. 32(b), the rise towards the value of 0.5 expected in the simple quark-parton model is very rapid.

The inclusive data then rapidly approach the distributions expected in the simple quark model and then develop with energy in the manner expected by the AFGT. This behavior is remarkable considering that the bulk of the data are in the resonance region.

ACKNOWLEDGMENTS

*Present Address: Carnegie-Mellon University, Pittsburgh, Pennsylvania 15213.

†Present Address: University of Maryland, College Park, Maryland 20842.

[1] S. J. Barish *et al.*, Phys. Rev. D <u>16</u>, 3103 (1977).

[2] J. Campbell *et al.*, Phys. Rev. Lett. <u>30</u>, 335 (1973); S. J. Barish *et al.*, *ibid.* <u>36</u>, 179 (1976).

[3] V. Barnes *et al.*, in *Neutrinos—78*, proceedings of the International Conference on Neutrino Physics and Astrophysics, Purdue, 1978, edited by E. C. Fowler (Purdue Univ. Press, Lafayette, Indiana, 1978), p. 217.

[4] P. Schreiner, in *Proceedings of the International Neutrino Conference, Aachen, 1976*, edited by H. Faissner, H. Reithler, and P. Zerwas (Vieweg, Braunschweig, West Germany, 1977), p. 333.

[5] P. Schreiner and F. von Hippel, Nucl. Phys. <u>B58</u>, 333 (1973).

[6] S. Adler, Ann. Phys. (N.Y.) <u>50</u>, 189 (1968).

[7] P. Zucker, Phys. Rev. D <u>4</u>, 3350 (1971).

[8] P. Salin, Nuovo Cimento <u>48A</u>, 506 (1967).

[9] J. Bijtebier, Nucl. Phys. <u>B21</u>, 158 (1970).

[10] For most of our energy range, $q_{\text{min}}^2 \sim 0.01$ $(\text{GeV}/c)^2$. The lowest q^2 bin was therefore chosen as 0.01–0.05 $(\text{GeV}/c)^2$.

[11] See, for example, K. Kubodera *et al.*, Phys. Rev. Lett. <u>38</u>, 321 (1977). Later experiments are consistent with no second-class term as discussed in T. J. Bowles and G. T. Garvey, Phys. Rev. C <u>18</u>, 1447 (1978).

[12] B. Holstein and S. B. Treiman, Phys. Rev. D <u>13</u>, 3059 (1976).

[13] A. Pais, Phys. Rev. D <u>5</u>, 1170 (1972).

[14] S. J. Barish *et al.*, Phys. Rev. Lett. <u>33</u>, 1446 (1975).

[15] M. Derrick *et al.*, Phys. Rev. D <u>17</u>, 1 (1978).

[16] D. H. Perkins, P. Schreiner, and W. Scott, Phys. Lett. <u>67B</u>, 347 (1977).

[17] W. Krenz, in *Proceedings of the International Neutrino Conference, Aachen, 1976* (Ref. 4), p. 385.

[18] T. Eichten *et al.*, Phys. Lett. <u>46B</u>, 274 (1973); S. J. Barish *et al.*, *ibid.* <u>66B</u>, 291 (1977).

[19] R. D. Field and R. P. Feynman, Phys. Rev. D <u>15</u>, 2590 (1977).